Journal of
Materials Chemistry B

Materials for biology and medicine

Accepted Manuscript

This article can be cited before page numbers have been issued, to do this please use: J. Wei, D. Zhang, Y. Chang, A. B. Santi, A. Gomez, L. Wang, G. Romero and J. Zheng, *J. Mater. Chem. B*, 2026, DOI: 10.1039/D5TB02063H.

ROYAL SOCIETY OF CHEMISTRY

rsc.li/materials-b

View Article Online
DOI: 10.1039/D5TB02063H

Freezing-Induced Ice–Polymer Structuring Enables Tough, Additive-Free Hydrogels Under Extreme Cold Conditions

Jialun Wei[1], Dong Zhang[2], Yung Chang[3], Athena B Santi[1], Amanda Gomez[1], Lijin Wang[1], Gabriela Romero Uribe[1], Jie Zheng[1]*

[1]Department of Biomedical Engineering and Chemical Engineering, The University of Texas at San Antonio, Texas 78249, USA

[2]The Wallace H. Coulter Department of Biomedical Engineering, Georgia Institute of Technology, Georgia 30332, USA

[3]R&D Center for Membrane Technology and Department of Chemical Engineering, Chung Yuan Christian University, Chung-Li 32023, Taiwan

* E-mail: jie.zheng@utsa.edu

View Article Online
DOI: 10.1039/D5TB02063H

Abstract

Designing hydrogels that retain mechanical robustness under subzero conditions remains a major challenge for applications in bioengineering, soft robotics, and extreme-environment systems. In this study, we introduce a fundamentally new strategy for creating tough frozen hydrogels by transforming ice—traditionally regarded as a brittle and damaging phase—into a functional, load-bearing component. Through the in situ formation of ice crystals within a fully physically crosslinked double-network (DN) hydrogel, ice is redefined from a transient structural template to an intrinsic reinforcing phase. The resulting frozen hydrogels exhibit remarkable stretchability, flexibility, and fracture resistance, even at cryogenic temperatures as low as -196 °C. Unlike conventional approaches that rely on nanofillers or cryogel templating followed by ice removal, this additive-free method harnesses directional freezing to achieve uniform ice–polymer structuring. Mechanistically, embedded ice crystals act as sacrificial energy-dissipating domains, enhancing toughness via interfacial debonding, microcrack deflection, and crack path redirection. This approach circumvents the dispersion and interfacial limitations of nanocomposites and establishes a scalable design paradigm for next-generation ice-reinforced soft composites capable of operating under extreme thermal conditions.

View Article Online
DOI: 10.1039/D5TB02063H

1. Introduction

Hydrogels, as soft and water-rich materials (50–90% water) comprising three-dimensional polymer networks, exhibit varied functions—such as stimuli-responsiveness[1, 2], ionic/electronic conductivity[3, 4], antifouling properties[5, 6], tunable mechanical strength[7, 8], low immunogenicity[9], and cell/tissue biocompatibility[10, 11], enabling applications in soft actuators[12, 13], wearable electronics[14, 15], tissue scaffolds[16], energy devices[17, 18] and drug delivery[19, 20]. At or near room temperature, conventional hydrogels generally perform well; under subzero conditions (≤ 0 °C), however, high-content water molecules confined in polymer networks tend to crystallize into small ice crystals that embrittle the polymer networks[21] and consequently degrade key functions, such as conductivity, transparency, elasticity, and flexibility[22-24], thereby limiting their uses in cold environments. Mechanistically, ice growth dehydrates the polymer network as water migrates to the crystals, generating internal stresses that damage the polymer skeleton and reduce mechanical performance[25]. Accordingly, polymer–water interactions at subzero temperatures are central to hydrogel performance—governing both structure and mechanics[15, 16]—yet remain underexplored.

Nevertheless, freezing is not necessarily detrimental to hydrogel structure or function. Under controlled conditions, several studies have demonstrated that water crystallization can be harnessed to engineer beneficial microstructures within hydrogels[26-28], offering a versatile strategy for tailoring hydrogel properties. Freeze-induced phase separation is a commonly used approach to prepare cryogels[29, 30] and ice-templated gels[31-33]. In these systems, freezing–thawing cycles play a dual role: redistributing polymer chains and using ice crystals as physical templates. During the freezing process, phase separation occurs as water begins to crystallize. By tuning parameters such as the cooling rate and freezing direction, the morphology of ice crystals—size, orientation, and distribution—can be modulated to form ordered and controllable architectures[34-36]. These crystals impose spatial constraints that guide the polymer network into defined geometries, effectively "templating" the developing structure. Upon thawing, the ice crystals melt and are removed, leaving behind an interconnected porous matrix. This engineered porosity greatly enhances several functional properties of the hydrogel, including increased permeability[37, 38], faster swelling kinetics[29], and improved mechanical robustness[27, 33].

In traditional cryogels and ice-templated hydrogels, ice crystals primarily act as transient templates. Once the desired porous architecture is formed, the ice is removed during thawing, leaving behind a structured polymer network. However, from a composite materials perspective, ice has the potential to serve a dual role—not only as a structural template but also as a reinforcing filler. Building on this concept, we hypothesize that if the underlying polymer network is sufficiently robust and tough, it can withstand the internal stresses caused by polymer dehydration during freezing. In such a system, rather than being melted and discarded, ice crystals can be retained within the hydrogel matrix. In this frozen state, the ice phase may function analogously

View Article Online
DOI: 10.1039/D5TB02063H

to reinforcing fillers—such as particles or short fibers—commonly used in composite materials[39, 40]. Hypothetically, retaining ice crystals within the tough polymer matrix (rather than melting them) could contribute to mechanical reinforcement through mechanisms such as interfacial energy dissipation, localized microcracking, or crack deflection. These processes could collectively enhance fracture resistance and toughness under mechanical deformation, offering a new paradigm in the design of subzero-tolerant hydrogels.

Unlike conventional nanoscale fillers, ice crystals could offer a uniquely effective strategy for reinforcing hydrogels—with perfect in situ dispersion, seamless compatibility, and tunable architecture achieved without added chemicals or complex processing. Conventional strategies to reinforce hydrogels typically rely on nanoscale additives such as carbon-based[41], metallic[42, 43], or cellulose-derived[44, 45] particles and fibers. While these fillers can improve mechanical strength, their uses often come with intrinsic challenges: poor dispersion due to hydrophobicity or agglomeration, phase separation during gelation or swelling, and weak interfacial interactions that limit efficient stress transfer. As a result, these nanofiller hydrogels frequently introduce heterogeneities and yield only modest or inconsistent mechanical gains.

To test our hypothesis that ice crystals can simultaneously serve as structural templates and reinforcing nanofillers to enhance hydrogel mechanics, we designed and synthesized a fully physically crosslinked double-network (DN) hydrogel composed of gelatin as the first network and poly (N-acryloyl glycinamide) (pNAGA) as the second network. The DN architecture was chosen because its tightly crosslinked network structure offers a more uniform and constrained mesh environment, which facilitates homogeneous nucleation and dispersion of ice crystals, resulting in more effective reinforcement at the nanoscale. Critically, the fully physical crosslinking of both networks—gelatin via thermally reversible triple helices and pNAGA via hydrogen bonding—distinguishes this DN system from other tightly crosslinked architectures. Whereas densely crosslinked covalent networks are inherently brittle under freeze-induced stresses because chain scission is irreversible, the non-covalent junctions in our DN hydrogel serve as sacrificial, reformable crosslinks that enable progressive energy dissipation while preserving backbone integrity. Moreover, the two networks fulfill complementary mechanical roles—gelatin providing structural elasticity and pNAGA providing load-bearing toughness—a hierarchical division of labor that a single tightly crosslinked network cannot achieve regardless of crosslink density. Unlike conventional strategies that rely on external nanoscale fillers—often requiring surfactants, surface functionalization, and complex dispersion techniques—our approach leverages water, an intrinsic component of hydrogels, as the precursor to an in situ reinforcing phase. Through controlled freezing, water is converted into uniformly distributed ice crystals that act both as physical templates during phase separation and as embedded reinforcements within the tough polymer matrix. Although bulk ice is macroscopically brittle due to its polycrystalline structure and defect-prone morphology[46], we hypothesize that when confined within a robust DN network, these

View Article Online
DOI: 10.1039/D5TB02063H

crystals act as sacrificial, energy-dissipating domains. Toughening mechanisms such as localized ice fracture, interfacial debonding, and crack deflection at the ice–polymer interface help resist catastrophic failure. As a result, gelatin/NAGA DN hydrogels exhibited superior mechanical properties at subzero temperatures compared to those at room temperature. In addition, the hydrogel's well-defined subzero transition enables two representative low-temperature demonstrations: a fluorescence-based temperature indicator and a supercooled, cytocompatible matrix for cell culture and preservation. This unexpected performance demonstrates the reinforcing role of ice crystals when embedded within a tough, physically crosslinked matrix. Fundamentally, this work offers a new perspective on the role of ice—not as a transient phase to be eliminated, but as a functional and tunable reinforcement component that enhances toughness through controlled microcracking and interfacial energy dissipation. Technically, our approach introduces a simple yet effective method for hydrogel reinforcement by leveraging water's natural phase transition to form *in situ* ice fillers without additives, surfactants, or post-synthesis processing. Together, these insights expand the conceptual and practical knowledge for designing high-performance hydrogels for cold-environment applications.

2. Materials and Methods

2.1 Materials

Gelatin (type A, gel strength ≈ 300 g/cm2), N-acryloyl glycinamide (NAGA, 98%) and 2-Hydroxy-4′-(2-hydroxyethoxy)-2-methylpropiophenone (I2959, 99%) were purchased from Sigma-Aldrich Inc. 8-anilinonaphthalene−1-sulfonic acid (ANS) was purchased from Fisher Scientific. Deionized water was purified by a Millipore water purification system, obtaining a resistivity of 18 MΩ cm. Uppsala 87 malignant glioma cell line (U87MG) was purchased from ATCC. Complete DMEM culture medium was prepared by supplementing DMEM (Corning) with 10% fetal bovine serum (FBS, Corning) and 1% penicillin–streptomycin (Gibco).

2.2 Hydrogel Synthesis

The synthesis method is adapted from one-pot method previously reported[47]. All materials of gelatin (0.8 g), NAGA (3.84 g), I-2959 (67.3 mg) and water (10 mL) were added to a tube, heated to 60 °C for 20 min to obtain a clear precursor solution. The precursor was injected into a mold, which was made by two pieces of glass slides separated by 1 mm PTFE spacer. The glass slides were covered by PET thin film for easier demolding. The sample was then put into a 2 °C refrigerator for 1 hour to create gelatin first network. Then, the mold was placed under UV light (UVP Crosslinker CL−1000L) for 90 mins to form second network. The obtained sample was carefully sealed by plastic wrap and stored in a 2 °C refrigerator. Before mechanical test, the sample was taken out for at least 15 min to reach room temperature.

2.3 Frozen hydrogel preparation

Basically, as-prepared samples were placed flat into freezing environments with

View Article Online
DOI: 10.1039/D5TB02063H

constant temperature to create the ice crystals. Plastic wrap was used to prevent ice growth from moisture in air. For the freezing time effect shown in **Fig. 4**, the sample was promptly removed after the designated freezing period and immediately tested. For the freezing temperature effect shown in **Fig. 5**, the sample was placed at freezer (-25 °C and -40 °C), dry ice-alcohol bath (-78 °C) and liquid nitrogen (-196 °C), for a sufficient duration to ensure reaching fully frozen state.

2.4 Mechanical Test

All mechanical Tests were performed on a universal tensile test machine (Instron 3345, MA). The sample was cut from sheet with 1 mm thickness, into dumbbell shape with width of 4 mm and gauge length of 10 mm. Pure shear tests were conducted on notched samples (10 mm × 20 mm, 1 mm thickness), with a 5 mm edge notch in the center created by a sharp knife. All tests were performed at a constant stretch rate of 100 mm/min unless otherwise specified.

To avoid any ambiguity regarding the thermal state of the samples, we explicitly differentiate the preparation temperature, testing environment, and specimen temperature. The preparation (freezing) temperature was precisely controlled at −20, −40, −78, or −196 °C to tune ice-crystal size and morphology. Although all mechanical tests were conducted under room-temperature ambient conditions, the specimen temperature during testing was the critical parameter. Samples were transferred directly from the freezer or cold bath to pre-cooled detachable grips (−40 °C) and tested within 10–15 s of removal. Real-time thermal imaging (FLIR E54) in **Fig. S1** confirmed that even ~1 min after mounting, the central gauge region and gripped ends remained well below 0 °C (typically −40 °C to −5 °C in the gauge section). Noticeable surface warming occurred only after necking or fracture—well after the key mechanical events (yielding, ice fracture, strain hardening) had taken place. Thus, the reported ultra-high strength, toughness, and ice-templated sacrificial mechanisms faithfully represent the intrinsic behavior of the frozen state rather than that of a partially or fully thawed hydrogel.

2.5 Infrared Thermal Imaging

Temperature changing profile of frozen hydrogels was recorded by thermal imaging camera (FLIR E54). As-prepared samples were first cut into disk with 10 mm diameter and 1 mm thickness, then using the same procedure to prepare frozen hydrogels. Frozen samples were then taken out and IR video was recorded in room temperature.

2.6 Scanning Electron Microscopy

The morphologies of frozen hydrogels were characterized by scanning electron microscope (JEOL 7401). Frozen hydrogels were fully freeze-dried. A thin layer of platinum was sputtered onto the sample for better contrast.

2.7 Optical Microscopy

The microscopic morphology of hydrogels frozen at different temperatures was

View Article Online
DOI: 10.1039/D5TB02063H

examined using an optical microscope (Echo Revolve4 Microscope). Hydrogels were first frozen under different temperatures to form frozen hydrogels. After freezing, the samples were thawed at room temperature, and their surface and internal morphologies were immediately observed. The pore structures visualized correspond to regions previously occupied by ice crystals.

2.8 Fluorescence and Temperature Sensing Measurement

80 μM of ANS was dissolved into the precursor solution prior to hydrogel fabrication. DN hydrogels were synthesized following the same preparation procedure described above, yielding homogeneous ANS-loaded samples. Fluorescence measurements were performed on hydrogel specimens (1 mm thick) placed on a temperature-controlled cold environment at -55 °C. The samples were cooled from room temperature, during which fluorescence images were recorded under a handheld UV LED (365 nm, 5W). Temperature profile during cooling was monitored using IR thermal imaging camera in real time.

2.9 Cell Viability Study

U87MG cells were seeded in 35 mm culture dish at density of 1.5×10^5 cells/mL. Cells were cultured for 48 h at 37 °C and 5% CO_2 before viability analysis. Gelatin/pNAGA DN hydrogels were synthesized directly in 35 mm culture dish at composition of $C_{gelatin}$ = 120 mg/mL and C_{NAGA} = 3 M. The discs were controlled at a thickness of 0.5 mm and sterilized by UV for 30 min before applying. Three experimental groups were prepared: (i) Control: cells cultured in fresh culture medium. (ii) Control-FT: cells cultured in medium and undergone one freeze–thaw cycle. (iii) Hydrogel-FT: cells covered with a gelatin/pNAGA DN hydrogel disc prior to the freeze–thaw cycle. For the freeze–thaw cycle, cell culture medium (with or without hydrogel overlay) was placed at 4 °C for 30 min and -20 °C for 1 h, then thawed at room temperature for another 30 min. Cell viability was assessed using a LIVE/DEAD staining kit (Invitrogen) following the manufacturer's instructions. Samples were washed with PBS and stained for 15 min at room temperature. Fluorescence images were collected using a fluorescence microscope (Nikon Eclipse Ti, Andor Zyla sCMOS). The percentage of viable cells was quantified by counting live (green) and dead (red) cells in ImageJ.

3. Results and Discussion

3.1. One-Pot Fabrication of Gelatin/pNAGA Double-Network Hydrogels in As-Prepared and Frozen States

As a proof of concept, we designed and synthesized gelatin/pNAGA double-network (DN) hydrogels using a one-pot, heating–cooling–photopolymerization process[48]. In **Fig. 1a**, all components—including gelatin, N-acryloyl glycinamide (NAGA, monomer), Irgacure 2959 (photo initiator), and water—were mixed in a single vessel and heated to 60 °C for approximately 20 minutes to yield a homogeneous, transparent solution. At this elevated temperature, gelatin chains were fully solubilized. The solution was then gradually cooled to 2 °C in 1 hour, during which the gelatin underwent a sol-to-gel transition, forming triple-helix structures that established the

View Article Online
DOI: 10.1039/D5TB02063H

physically crosslinked first network. This was followed by ultraviolet (UV) irradiation for 1.5 hours, initiating the free-radical polymerization of N-acryloyl glycinamide (NAGA) and resulting in the formation of the second network. Notably, this DN hydrogel system does not involve any chemical crosslinkers. Instead, both networks are physically crosslinked: the first via gelatin's reversible triple helices, and the second via strong hydrogen bonding between the amide groups in pNAGA chains[49]. This fully physical gelatin/pNAGA DN hydrogel provides a robust and dynamic framework ideal for testing our ice-based reinforcement strategy under subzero temperatures.

For comparison, the as-prepared hydrogel sample was placed in a controlled subzero environment at -25 to -196 °C to induce freezing. As shown in **Fig. 1b**, differential scanning calorimetry (DSC) analysis confirmed that, under a cooling rate of 5 °C/min, water within the hydrogel crystallized at approximately -20 °C to -25 °C, forming ice crystals. Ice formation in the polymer network is governed by a phase separation process, wherein water molecules aggregate and solidify, leading to progressive dehydration of the surrounding polymer chains. As the ice crystals grow, they exert compressive forces on the polymer matrix, inducing greater chain entanglement and enhancing network density through intensified intermolecular interactions. Throughout this freezing process, the physically crosslinked networks are able to dynamically adapt to the expansion of the ice phase, effectively mitigating localized stress concentrations that would otherwise arise from water crystallization. This structural adaptability is key to maintaining mechanical robustness in the frozen state. Optical images shown in **Fig. 1c** further illustrate the exceptional ductility of the frozen hydrogel, which remains flexible under large deformations. The material can be coiled, folded, or even knotted without fracture, demonstrating its outstanding toughness and structural integrity when frozen.

View Article Online
DOI: 10.1039/D5TB02063H

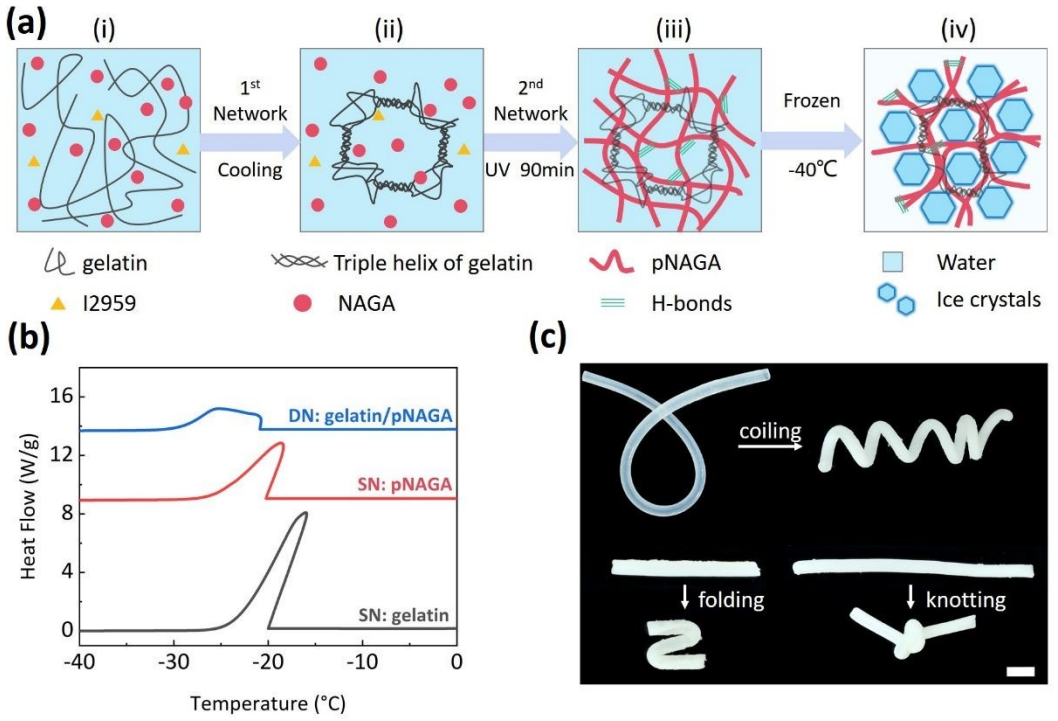

Fig. 1. (a) Schematic illustration of the synthesis process of gelatin/pNAGA double-network hydrogels in both the as-prepared and frozen states. (i) A precursor solution containing gelatin, N-acryloyl glycinamide (NAGA), and a photo initiator was heated to 60 °C and subsequently cooled to 2 °C to induce (ii) physical gelation of gelatin via a sol-to-gel transition, forming the first network. (iii) Upon exposure to UV light for 90 minutes, NAGA polymerized to form the second network, resulting in the DN hydrogel. (iv) The as-prepared DN hydrogel was then frozen to generate uniformly distributed ice crystals. **(b)** Differential scanning calorimetry (DSC) curves of single network (SN) and DN hydrogels, measured at a cooling rate of -5 °C/min. Crystallization peak of water was observed between -30 °C and -20 °C. **(c)** Optical images of frozen DN hydrogels under large mechanical deformation, showing excellent ductility through coiling, folding, and knotting without fracture.

3.2. Enhanced Mechanical Properties of Frozen DN Hydrogels Tuned by Network Composition

To assess the mechanical reinforcement provided by freezing, we systematically compared the mechanical properties of as-prepared and frozen gelatin/pNAGA double-network (DN) hydrogels by independently varying the compositions of both networks. Representative stress–strain curves illustrating the effects of pNAGA and gelatin content are shown in **Fig. 2a** and **2d**, respectively, with corresponding summaries of mechanical parameters presented in **Fig. 2b, 2c, 2e** and **2f**.

We first investigated the role of the pNAGA network by varying the concentration of NAGA (C_{NAGA}) from 1 M to 4 M. In the as-prepared hydrogels, maximum strain initially increased from 9.4 mm/mm at 1 M to 15.7 mm/mm at 3 M, followed by a

View Article Online
DOI: 10.1039/D5TB02063H

decrease to 11.5 mm/mm at 4 M. This non-monotonic trend reflects a balance between network extensibility and stiffness: increasing NAGA concentration up to 3 M enhances polymer chain density and stretchability through additional hydrogen bonding. However, further increasing the concentration to 4 M likely introduces excessive physical crosslinking, which restricts chain mobility and limits deformation. In parallel, frozen hydrogels, prepared at -40 °C, displayed a similar trend in strain, with a maximal strain of 17.5 mm/mm at an intermediate C_{NAGA} of 3 M. Notably, across the entire concentration range of 2 M to 4 M, frozen hydrogels consistently outperformed their as-prepared counterparts in terms of maximum strain. This enhancement is attributed to ice-driven energy dissipation mechanisms: during deformation, embedded ice crystals undergo microfracture and interfacial debonding, absorbing mechanical energy and shielding the polymer network from localized failure. At the lowest concentration (1 M), however, the frozen hydrogel showed the reduced strain capacity compared to higher concentrations. This is likely due to insufficient network density to accommodate the stresses introduced by ice growth and fracture.

In terms of stress and modulus, both properties increased steadily with rising C_{NAGA} for both as-prepared and frozen hydrogels, with the frozen hydrogels consistently exhibiting superior performance. Specifically, as C_{NAGA} increased from 1M to 4M, the stress of the as-prepared hydrogels rose from 0.4 MPa to 1.7 MPa, while the corresponding frozen hydrogels exhibited higher stress values ranging from 0.75 MPa to 2.25 MPa. Such stress enhancement reflects two synergistic effects: (1) improved network entanglement and hydrogen bonding in the DN structure, and (2) mechanical reinforcement from ice crystals, which demand additional energy for fracture and interfacial disruption during tensile loading. The modulus was also consistently elevated in the frozen hydrogels (**Fig. S2**). Compression tests further confirmed this trend, where frozen hydrogels exhibited consistently higher stress compared to as-prepared counterparts across C_{NAGA} values (**Fig. S3**). This is attributed to freeze-induced phase separation, which dehydrates and compacts the polymer matrix, forming a denser and more glass-like network. Additionally, since ice possesses a much higher intrinsic modulus than liquid water, its incorporation as a dispersed solid phase further contributes to stiffness. The synergistic interaction between ice and polymer results in a hybrid material with markedly improved modulus and stress-bearing capacity.

To further evaluate the structural contributions of the first network, we investigated the effect of gelatin concentration ($C_{gelatin}$) on the tensile behavior of both as-prepared and frozen gelatin/pNAGA DN hydrogels. In both hydrogel states, increasing $C_{gelatin}$ from 0 to 160 mg/mL led to a general rise in tensile stress, with only moderate effects on strain (**Fig. 2b-c** and **e-f**). For as-prepared hydrogels, the maximum tensile strain remained relatively stable in the range of 20–25 mm/mm at lower gelatin concentrations (0–80 mg/mL), while the tensile stress increased gradually, reaching approximately 2 MPa at the highest gelatin concentration of 160 mg/mL. Frozen hydrogels exhibited a comparable strain range but consistently demonstrated higher

View Article Online
DOI: 10.1039/D5TB02063H

tensile stress, with values increasing to 2.3 MPa at 120 mg/mL and up to 2.5 MPa at 160 mg/mL. These results suggest that while gelatin concentration contributes to improved stress-bearing capacity, its impact on extensibility is limited—likely due to the relatively short and reversible nature of gelatin's triple-helix crosslinking. Importantly, frozen hydrogels again outperformed as-prepared samples across all tested gelatin concentrations. The stress enhancement is attributed to the formation of ice crystals, which act as embedded reinforcing domains. These crystals increase stiffness (**Fig. S4**) through physical confinement and enhance toughness by promoting energy dissipation via localized ice fracture and interfacial sliding during tensile loading.

At first glance, however, the mechanical enhancement achieved by varying gelatin concentration is notably less pronounced than that observed with changes in pNAGA content. This difference reflects the distinct roles of the two networks: the gelatin network primarily provides a structural scaffold and basic elasticity, while the pNAGA network—rich in hydrogen-bonding motifs—forms a denser, more load-bearing phase. As a result, increasing C_{NAGA} introduces a more significant rise in polymer–polymer interactions and crosslink density, leading to greater improvements in both stress and strain. In contrast, the gelatin network reaches a mechanical plateau due to the saturation of physical crosslinking and its weaker interchain forces.

View Article Online
DOI: 10.1039/D5TB02063H

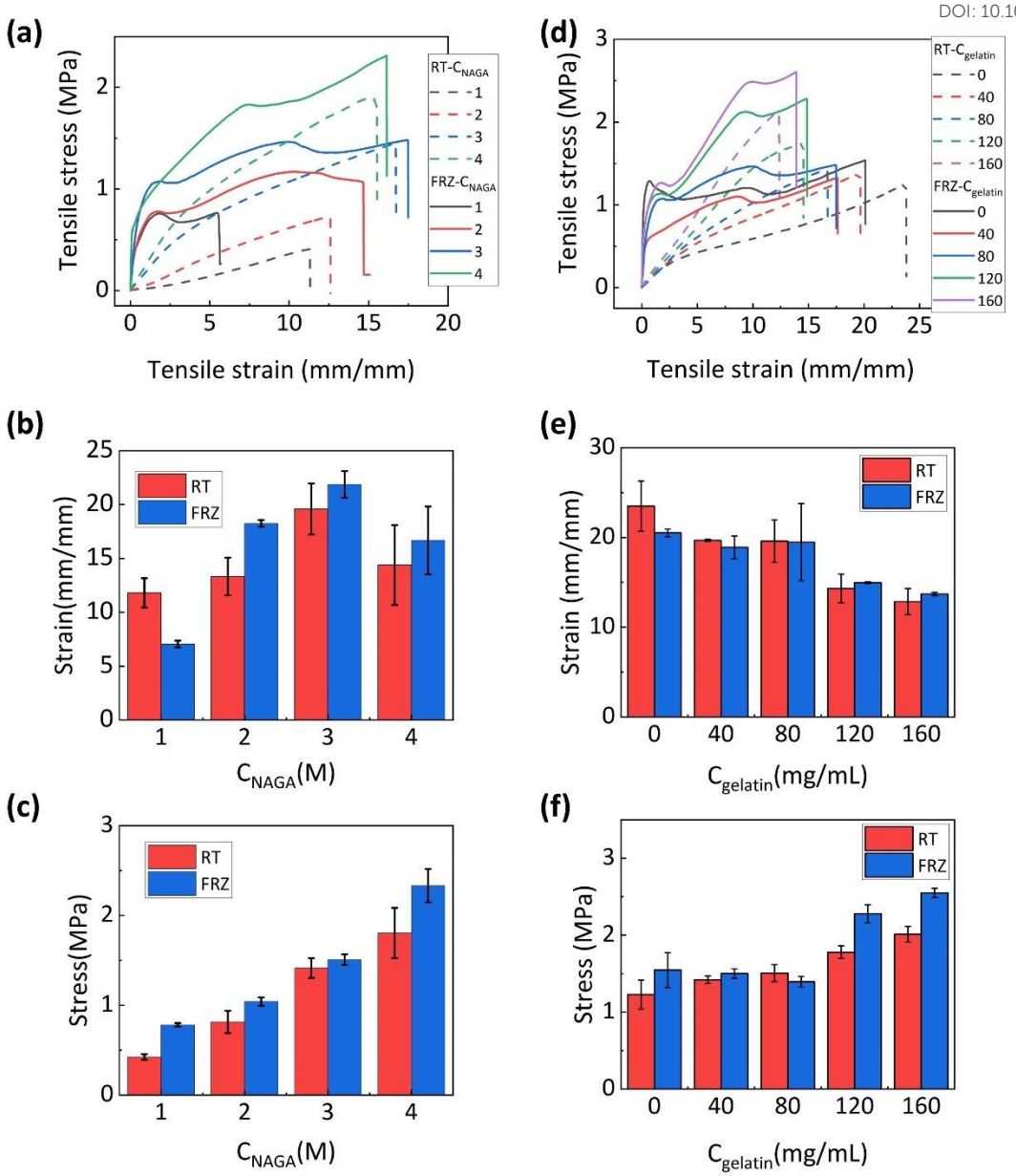

Fig. 2. Tensile mechanical comparison between gelatin/pNAGA hydrogels at room temperature (RT) and in the frozen state (FRZ). (a) Representative stress–strain curves of as-prepared (dashed lines) and frozen (solid lines) hydrogels with varying concentrations (C_{NAGA}=1–4 M). Corresponding **(b)** maximum tensile strain and **(c)** tensile stress as a function of C_{NAGA}. **(d)** Representative stress–strain curves of as-prepared (dashed lines) and frozen (solid lines) hydrogels with varying gelatin concentrations ($C_{gelatin}$=0–160 mg/mL). Corresponding **(e)** maximum tensile strain and **(f)** tensile stress as a function of $C_{gelatin}$. Error bars represent standard deviation (n = 3).

To assess operational robustness, we performed the freeze–thaw cycling on gelatin/pNAGA DN hydrogels, alternating between room temperature (RT) and -40 °C freezing temperature (FRZ) states for five cycles, with tensile tests after each state change (**Fig. 3**). To isolate the effect of cycling from dehydration, samples were sealed

View Article Online
DOI: 10.1039/D5TB02063H

during testing, and mass was monitored (Δm < 0.2% across cycles). As shown in **Fig. 3a**, the stress–strain curves after each cycle nearly overlap in both RT and FRZ states, indicating highly reversible and reproducible mechanical behavior. Quantitatively, at RT the tensile stress remains 1.25–1.39 MPa, fracture strain 14.4–15.2 mm/mm, and modulus 0.10–0.22 MPa; in the FRZ state the stress is 1.44–1.55 MPa, strain 10.3–11.4 mm/mm, and modulus 2.3–3.3 MPa (**Fig. 3b**). A slight increase in tensile stress over the first few cycles in both states suggests incremental optimization of hydrogen-bonded domains during repeated ice formation, after which mechanical properties stabilize. These data demonstrate that the ice-enabled reinforcement is reversible and reproducible over multiple RT↔FRZ transitions, with no cumulative degradation in strength, extensibility, or modulus in either state.

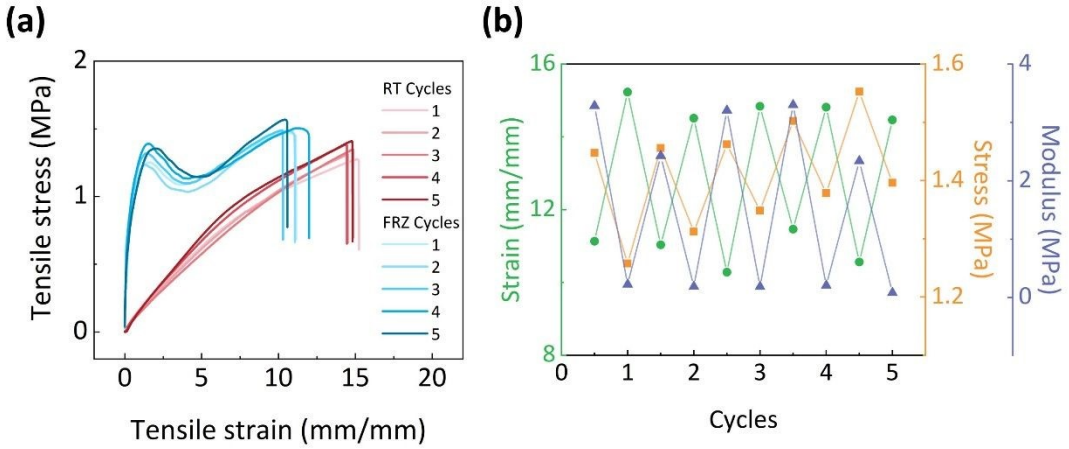

Fig. 3. Freeze–thaw cycling of gelatin/pNAGA DN hydrogels prepared at C_{NAGA}=3 M and $C_{gelatin}$=80 mg/mL between room temperature (RT) and -40 °C freezing temperature (FRZ). (a) Tensile stress–strain curves measured after each of five cycles between RT and FRZ states. FRZ state exhibits higher modulus and stress, but lower strain than RT, demonstrating state-dependent reinforcement. **(b)** Extracted mechanical strain (green), stress (orange), and modulus (purple) vs. cycle demonstrate reversible, reproducible oscillation between the two states, confirming robust, reversible reinforcement without cumulative drift.

The dynamic, reversible nature of the physical crosslinks—gelatin triple helices and pNAGA hydrogen bonds—is essential for the ice-based toughening mechanism. During freezing, these non-covalent junctions can reorganize to accommodate volumetric expansion from ice crystallization; during deformation, they serve as sacrificial bonds that dissipate energy while preserving backbone integrity. To examine what happens when covalent crosslinks are introduced, we prepared DN hydrogels containing varying concentrations of the chemical crosslinker MBAA (0–0.5%) and compared their tensile performance at both room temperature and −40 °C (**Fig. S5**).

The results clearly demonstrate that covalent crosslinking suppresses the freezing-induced reinforcement. At 0% MBAA (purely physical crosslinking), frozen hydrogels

View Article Online
DOI: 10.1039/D5TB02063H

exhibit a tensile strain of ~22 mm/mm—substantially exceeding the RT value of ~18 mm/mm—confirming the ice-enabled toughening effect (**Fig. S5b**). However, as C_MBAA increases, both strain and stress decline sharply under both conditions (**Fig. S5b–c**), and the enhancement gap between frozen and RT states progressively narrows. At 0.5% MBAA, strain collapses to ~3 mm/mm regardless of temperature, indicating that the permanent covalent junctions restrict chain mobility and suppress the large-scale network reorganization required for effective ice–polymer structuring. In other words, the covalent crosslinks prevent the polymer matrix from dynamically adapting to ice formation, thereby eliminating the sacrificial energy-dissipation mechanisms that underpin the freezing-induced reinforcement.

3.3. Freezing-Induced Ice Morphology and Network Reorganization in DN Hydrogels

To better understand the freezing-induced toughening mechanisms of DN hydrogels, particularly in relation to ice formation and phase behavior, a series of systematic experiments were conducted using gelatin/pNAGA hydrogels prepared at C_{NAGA}=3 M and $C_{gelatin}$=80 mg/mL, which exhibited optimal mechanical performance in prior tests. These studies aimed to evaluate how different freezing parameters influence the mechanical properties and energy dissipation capacity of frozen hydrogels. Specifically, two experimental conditions were designed: (1) maintaining a constant freezing temperature while varying the freezing duration to investigate the temporal development of ice crystals within the network, and (2) exposing the hydrogels to different subzero environmental temperatures to achieve varying cooling rates, thereby examining how temperature gradients affect the phase separation behavior between ice and the polymer matrix.

First, to examine how freezing time affects mechanical reinforcement, **Fig. 4a** shows stress–strain curves of gelatin/pNAGA DN hydrogels, prepared at fixed composition of C_{NAGA}=3 M and $C_{gelatin}$=80 mg/mL and frozen at -40 °C for varying durations (5, 10, 15, 20, and 30 minutes). As the freezing time increased from 5 to 20 minutes, tensile stress rose steadily from approximately 0.75 MPa to a peak of ~2.2 MPa, indicating progressive reinforcement of the network (**Fig. 4b**). This trend suggests that longer freezing durations allow for more extensive ice crystal growth and polymer phase reorganization, promoting stronger physical interactions between the ice and polymer network. Strain, on the other hand, remained relatively stable in the range of 15–20 mm/mm across all time points, with a slight increase at 15 minutes. The peak mechanical performance observed at 20 minutes suggests an optimal balance: sufficient ice–polymer phase separation and network densification are achieved without introducing excessive crystallinity or inhomogeneity. Beyond this point, particularly at 30 minutes, the tensile stress slightly declined, possibly due to overgrowth or coarsening of ice crystals, which may disrupt uniform load distribution or introduce stress concentration sites. These findings suggest that an optimal freezing duration exists (~20 minutes under -40 °C in this case), where ice formation is sufficient to reinforce the network without compromising structural homogeneity.

View Article Online
DOI: 10.1039/D5TB02063H

To probe the energy dissipation mechanisms of frozen DN hydrogels, cyclic tensile loading–unloading tests were conducted on samples frozen at -40 °C for varying durations (0, 5, and 30 minutes). The resulting stress–strain loops are shown in **Fig. 4c**, while the extracted energy values—both total and dissipated—are summarized in **Fig. 4d**. As freezing time increased, the area enclosed by the hysteresis loop (representing dissipated energy) expanded substantially, indicating enhanced internal energy dissipation. Specifically, the hydrogel frozen for 30 minutes exhibited a much broader loop than those frozen for shorter durations or not frozen at all. Quantitative analysis in **Fig. 4d** shows that the dissipated energy increased markedly with freezing time, rising from approximately 65% of total loading energy in the unfrozen sample to nearly 91% after 30 minutes of freezing. For comparison, **Fig. S5** presents the cyclic loading–unloading behavior of DN hydrogels tested at room temperature. The total energy input also increased over time, suggesting that the frozen samples became not only more dissipative but also stiffer and more resistant to deformation. Again, this progressive enhancement in energy dissipation is attributed to the growing contribution of ice crystals embedded within the polymer network.

Additional cyclic tests under varying strain levels further confirmed the superior energy-dissipation capacity of the frozen DN hydrogels (**Figs. S6** and **S7**). As shown in **Fig. S6**, the mechanical responses under successive loading–unloading cycles with increasing maximum strain (from 1 to 5 mm/mm) reveal a clear evolution of dissipative behavior. In the initial low-strain cycles (1 and 2 mm/mm), large hysteresis loops were observed (**Fig. S6a**), indicating substantial energy absorption. However, the loop area progressively decreased in later cycles (3–5 mm/mm), suggesting that most sacrificial energy-dissipating mechanisms were activated early in the loading history. Quantitatively, the energy dissipation ratio exhibited a distinct two-stage trend: it remained high (~80%) during the first two cycles (1–2 mm/mm), corresponding to the fracture of rigid ice domains, and then decreased to a steady range of 50–58% at higher strains (3–5 mm/mm) (**Fig. S6b**). This transition implies that irreversible ice-crystal fracture dominates the early deformation stage, while subsequent loading increasingly depends on the recoverable elasticity of the polymer network, resulting in a reduced proportion of dissipated energy at higher strains.

As shown in **Fig. S7a**, the first cycle exhibits pronounced stress softening and an extraordinarily large hysteresis loop, with total toughness of 8.2 MJ/m^3 and a dissipation ratio (dissipated energy/total input energy) of 90%. This exceptionally high energy dissipation is attributed to widespread microfracture of sacrificial ice domains and interfacial debonding during the initial deformation. From the second cycle onward, both total toughness (~1.75 MJ/m^3) and dissipated energy drop sharply and then stabilize, yielding a dissipation ratio of ~47%–50% that remains essentially constant through cycles 3–5, with nearly overlapping stress–strain curves (**Fig. S7b**). The marked reduction in stiffness and hysteresis between the first and second cycles, followed by near-perfect recovery of the stress–strain loop shape in subsequent cycles,

View Article Online
DOI: 10.1039/D5TB02063H

is a hallmark of the Mullins effect typically observed in filled elastomers and soft materials containing sacrificial microstructures. This characteristic Mullins-like softening therefore indicates that the vast majority of fracture-susceptible ice crystallites and weak ice–polymer interfaces are irreversibly damaged in the very first cycle. Subsequent cycles are governed by reversible dissipation mechanisms (viscoelastic rearrangement of hydrogen bonds and interfacial friction/sliding at reformed ice–polymer interfaces) with negligible additional permanent damage. Notably, the stabilized dissipation ratio of the frozen hydrogel after the first cycle closely matches that measured for the same hydrogel in its unfrozen state under identical cyclic conditions, confirming that the residual energy-dissipation capacity originates primarily from the polymeric network rather than from intact ice reinforcement.

To visualize the microstructural and thermal evolution associated with freezing, both scanning electron microscopy (SEM) and infrared (IR) imaging were employed. These tools provide complementary insights into ice crystal morphology, polymer rearrangement, and melting behavior as functions of freezing time. As shown in **Fig. 4e**, SEM images of cryo-fractured hydrogel cross-sections—corresponding to different freezing durations—reveal the progressive growth of vertically aligned ice crystals. These structures exhibit a characteristic columnar morphology, resulting from the vertical temperature gradient during unidirectional freezing. Such directional growth is consistent with ice-templating mechanisms observed in freeze-cast hydrogel systems[50-52]. The growth of ice crystals induces local phase separation: water is expelled from polymer-rich domains, leading to progressive dehydration and densification of the polymer matrix. This dehydration triggers structural rearrangement of polymer chains, forming a denser, aligned network adjacent to the ice domains. As freezing proceeds toward equilibrium, a more compact, polymer-rich layer forms near the core. Similar dehydration-driven reorganization has been observed in dynamic hydrogel systems[53]. To further verify the evolution of ice morphology, IR thermographic imaging was conducted during the melting process under ambient conditions (**Fig. 4f**). Hydrogels frozen for 0, 5, and 30 minutes were rapidly quenched in liquid nitrogen to preserve the ice morphology and then allowed to thaw at room temperature. The thermal maps reveal slower melting in samples with longer freezing times—consistent with larger average ice crystal size and reduced surface-area-to-volume ratio. These results indicate that prolonged freezing promotes the formation of larger, more stable ice domains, which persist longer during thawing and contribute to enhanced mechanical stiffness and energy dissipation during deformation.

Together, these combined microstructural and macroscopic observations confirm that extended freezing time promotes the growth and integration of ice domains within the polymer network, enhancing phase separation and enabling energy-dissipating mechanisms—such as microcrack formation, interfacial sliding, and crack deflection—that collectively reinforce the toughness of frozen DN hydrogels.

View Article Online
DOI: 10.1039/D5TB02063H

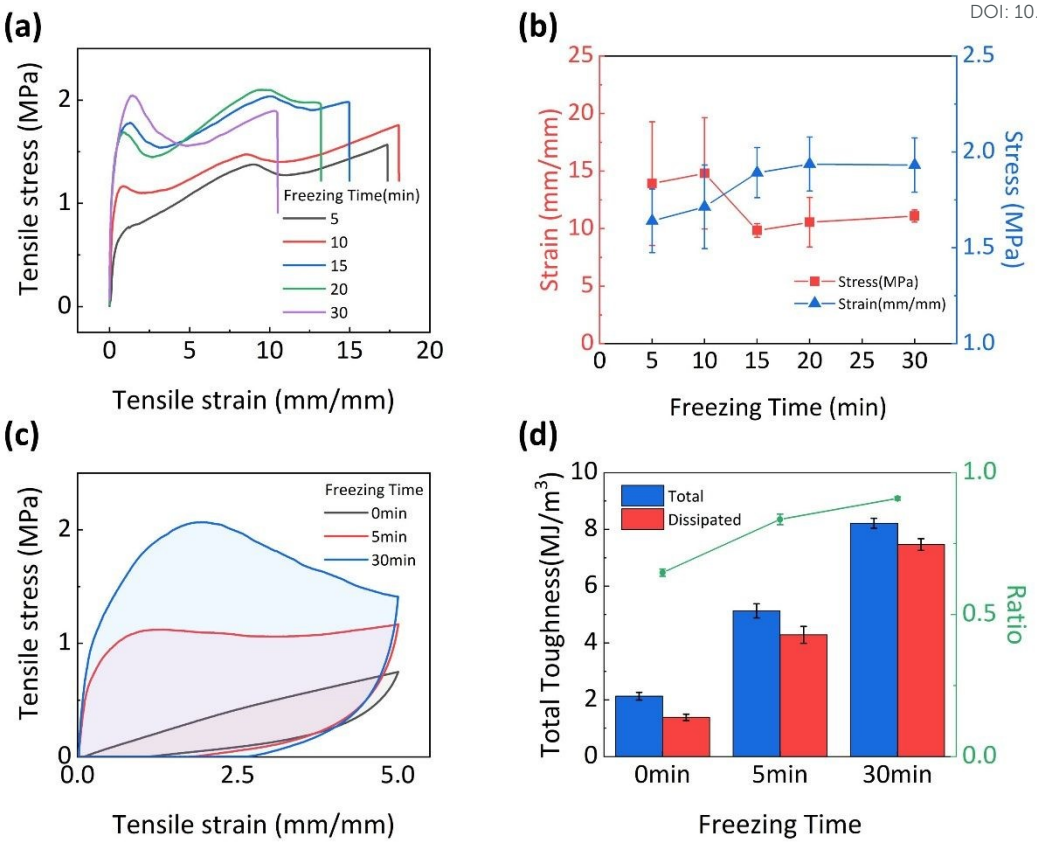

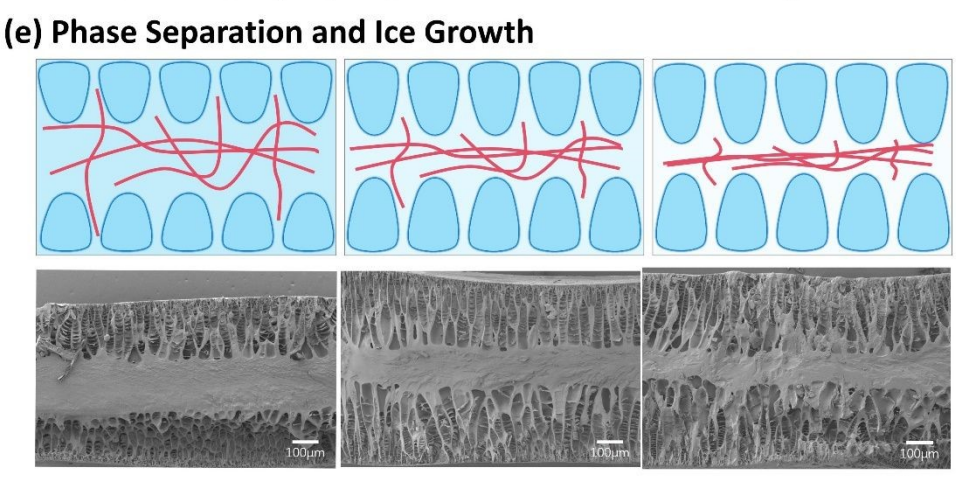

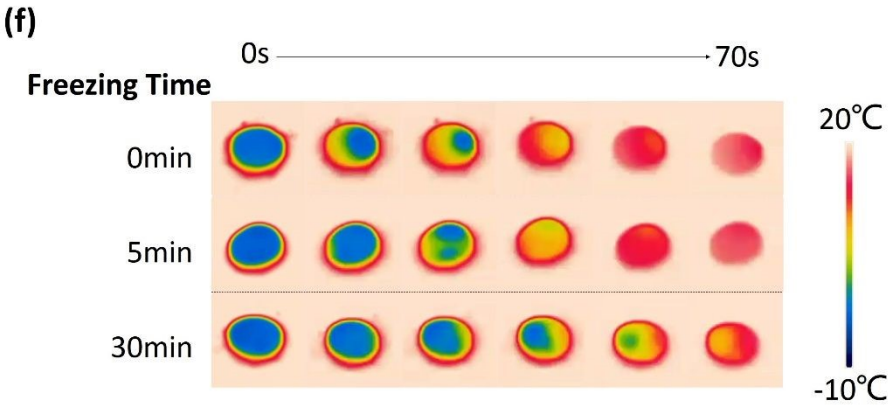

View Article Online
DOI: 10.1039/D5TB02063H

Fig. 4. (a) Tensile stress–strain curves of frozen gelatin/pNAGA DN hydrogels prepared at C_{NAGA}=3 M and $C_{gelatin}$=80 mg/mL and frozen at -40 °C for varying durations (5–30 minutes). **(b)** Corresponding maximum tensile stress (blue) and strain (red) as a function of freezing time. **(c)** Cyclic tensile loading–unloading curves of gelatin/pNAGA DN hydrogels frozen at -40 °C for different durations (0, 5, and 30 minutes). **(d)** Corresponding total energy (blue) and dissipated energy (red) extracted from stress–strain loops in (c), along with the energy dissipation ratio (green line, right axis). Error bars represent standard deviation (n = 3) in (b) and (d). **(e)** Schematic illustration (top) and SEM cross-sectional images (bottom) showing the phase separation and directional ice growth in gelatin/pNAGA DN hydrogels after freezing for different durations. Ice crystals grow vertically due to a surface-to-core temperature gradient, forming columnar morphologies and inducing dehydration-driven polymer densification. Scale bars = 100 μm. **(f)** Infrared (IR) thermal images showing the thawing behavior of frozen DN hydrogels at room temperature following freezing at -40 °C for 0, 5, and 30 minutes. Longer freezing times resulted in larger ice crystals, which melted more slowly due to reduced surface-area-to-volume ratios.

In parallel, we also investigated the role of freezing temperature on ice crystal formation and hydrogel mechanics of gelatin/pNAGA DN hydrogels, which were frozen at -25 °C, -40 °C, -78 °C, and -196 °C, followed by tensile tests (**Fig. 5a–b**) and cyclic loading–unloading tests (**Fig. 5c–d**). Because the hydrogel samples were placed directly into preset constant-temperature environments, the effective cooling rate scales with the magnitude of the temperature differential between the sample and its surroundings; thus, lower freezing temperatures correspond to faster cooling rates, establishing a direct link between environmental temperature, freezing kinetics, and the resulting ice morphology. As shown in **Fig. 5a**, lowering the freezing temperature slightly reduced the maximum tensile stress of the hydrogels—from ~2.0 MPa at -25 °C to ~1.8 MPa at -196 °C. This stress reduction is attributed to the formation of smaller ice crystals at lower temperatures, which apply more uniform but less concentrated compressive force on the polymer matrix. Because smaller crystals exert less localized mechanical compression, the network experiences reduced rearrangement and densification, leading to modest reinforcement compared to larger ice domains formed at higher freezing temperatures. Tensile strain exhibited a non-monotonic trend (**Fig. 5b**). Hydrogels frozen at -25 °C had the lowest strain (~9 mm/mm), likely due to the restriction of crack propagation by large, aligned ice crystals that promote brittle failure. The strain peaked at ~12 mm/mm for samples frozen at -40 °C, where intermediate crystal size allowed for localized energy dissipation and improved fracture resistance. Further reductions in freezing temperature (-78 °C and -196 °C) led to slightly lower strains (~11 mm/mm), likely due to reduced polymer rearrangement and chain entanglement, which limit the deformability of the network despite the presence of finer ice crystals. Cyclic loading–unloading tests (**Fig. 5c**) under a fixed strain (500%) revealed a clear increase in hysteresis loop area with decreasing temperature. Quantitative analysis of energy dissipation and total toughness (**Fig. 5d**) confirmed that lower freezing temperatures resulted in significantly greater energy dissipation—rising

View Article Online
DOI: 10.1039/D5TB02063H

from a total toughness of ~2.1 MJ/m^3 at room temperature to ~11.2 MJ/m^3 at -78 °C. Notably, the ratio of dissipated to total energy approached ~92% at the lowest temperatures, highlighting the dominant contribution of interfacial mechanisms to energy absorption.

As shown in **Fig. 5e**, SEM images of freeze-fractured cross sections reveal a dramatic reduction in average ice crystal size with decreasing freezing temperature—from approximately 50 μm at -25 °C to ~4 μm at -196 °C. This trend supports classical nucleation theory[54], which predicts that faster cooling induces higher nucleation rates, resulting in a greater number of nucleation sites and consequently smaller crystals due to limited growth time. At -25 °C and -40 °C, larger and more isolated ice domains are evident, producing well-defined pore structures. In contrast, samples frozen at -78 °C and -196 °C show a finer, more homogeneously distributed porous network, indicating widespread nucleation and constrained crystal growth. Complementary optical microscopy after thawing also revealed pore structures reflecting ice crystal size and distribution at different freezing temperatures (**Fig. S8**). The corresponding thermal behavior during thawing was monitored via IR imaging (**Fig. 5f**). All samples were equilibrated to -40 °C prior to thawing to ensure uniform initial conditions. As thawing proceeded at room temperature, samples with smaller ice crystals (formed at lower freezing temperatures) exhibited more rapid temperature recovery. This is attributed to their higher surface-area-to-volume ratios, which promote faster heat exchange and ice melting. In contrast, samples with larger ice domains (-25 °C and -40 °C) showed slower thermal responses, consistent with slower melting kinetics and greater thermal inertia.

Together, these results demonstrate that freezing temperature strongly influences both the microscale morphology of ice crystals and the macroscale thermal and mechanical response of frozen hydrogels. Rapid freezing at lower temperatures leads to the formation of finer and more uniformly distributed ice crystals, which increase the ice–polymer interfacial area and generate more fracture initiation sites. These microstructures enhance sacrificial toughening mechanisms—such as interfacial delamination and ice crystal fracture—thereby significantly improving energy dissipation and overall mechanical toughness. Additionally, the ability to tune ice crystal size through freezing rate has direct implications for tailoring not only mechanical performance but also recovery time during thawing in dynamic or temperature-variable environments.

View Article Online
DOI: 10.1039/D5TB02063H

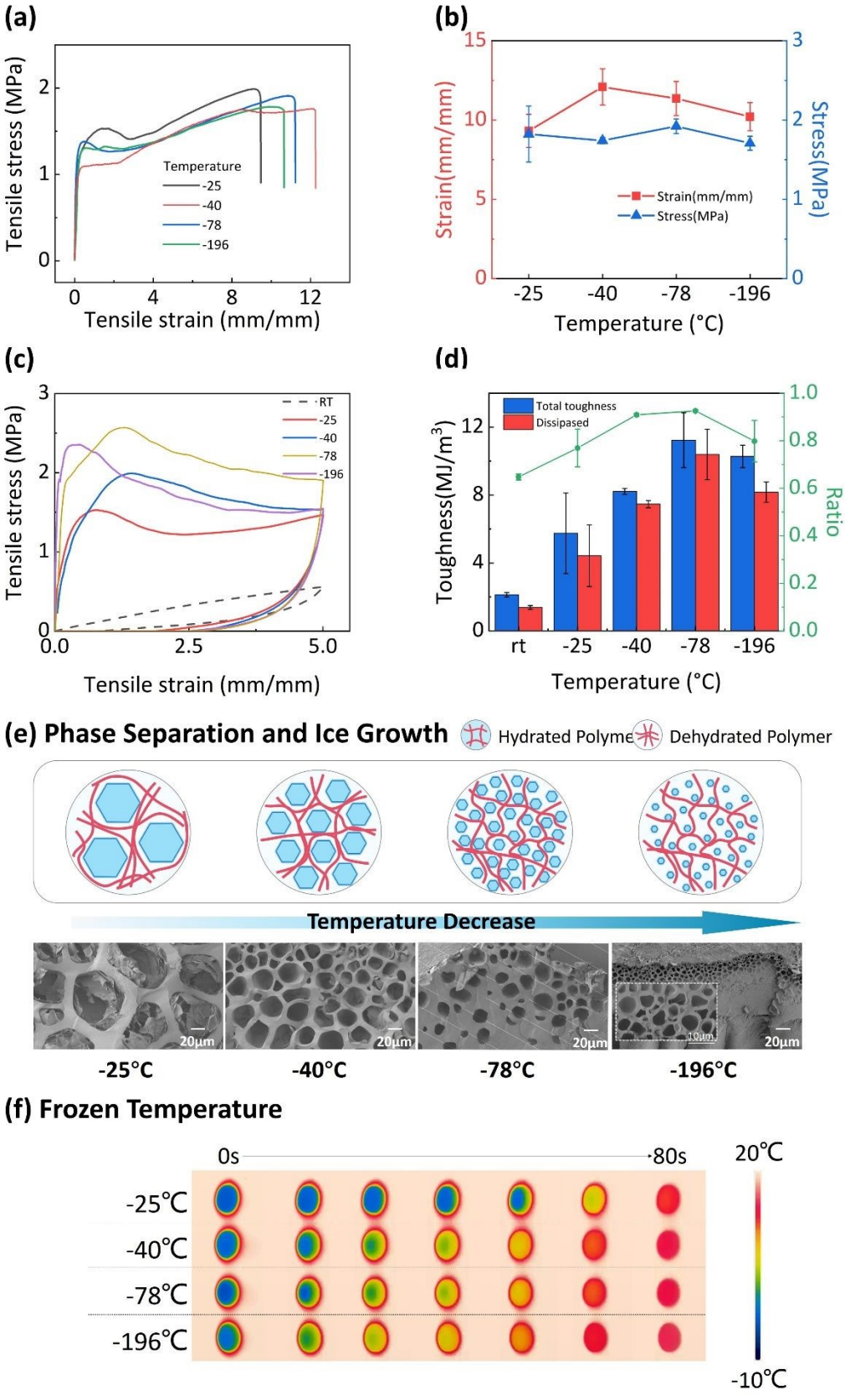

Fig. 5. (a) Stress–strain curves of frozen gelatin/pNAGA DN hydrogels prepared at C_{NAGA}=3 M and $C_{gelatin}$=80 mg/mL and various freezing temperatures (-25 °C to -

View Article Online
DOI: 10.1039/D5TB02063H

196 °C). **(b)** Extracted tensile stress (red, right axis) and strain (black, left axis) as functions of freezing temperature. **(c)** Cyclic loading–unloading curves under 500% strain, showing enhanced hysteresis with decreasing temperature. **(d)** Quantified total toughness (blue), dissipated energy (red), and energy dissipation ratio (green line, right axis). Error bars represent standard deviation (n = 3) in (b) and (d). **(e)** Schematic (top) and SEM images (bottom) showing the phase separation and ice crystal morphology of gelatin/pNAGA DN hydrogels frozen at different temperatures (-25 °C to -196 °C). Scale bars = 20 μm. (f) Infrared thermal images showing the thawing behavior of frozen hydrogels at room temperature after equilibration at -40 °C. Samples with smaller ice crystals (from lower freezing temperatures) melted more rapidly due to higher surface-area-to-volume ratios.

3.4. Fracture Mechanics and Toughening Mechanisms in Frozen DN Hydrogels

The structural analyses above demonstrate that freezing reorganizes the DN structure, generating ice–polymer architectures capable of efficiently dissipating mechanical energy. To elucidate the underlying fracture mechanics and specific toughening mechanisms of these frozen DN hydrogels, we conducted a comprehensive investigation integrating pure-shear testing, fracture morphology analysis, and rate-dependent mechanical characterization. First, we evaluate how ice crystal structure influences fracture behavior using pure shear tensile tests on notched gelatin/pNAGA DN hydrogels frozen at varying temperatures (-25 °C to -196 °C), in comparison with the same notched hydrogels at room temperature. In **Fig. 6a**, at room temperature, the DN hydrogel—lacking ice crystals—exhibited a typical crack blunting response during deformation. This behavior is characteristic of physically crosslinked DN systems, where dynamic hydrogen bonds enable local network reorganization. Upon crack initiation, these reversible interactions can temporarily dissipate energy and redirect stress fields, effectively delaying crack propagation. In contrast, frozen DN hydrogels displayed markedly different fracture behavior. As freezing temperature decreased, the overall crack resistance improved significantly. The maximum strain at break increased from ~1.4 mm/mm at -25 °C to ~6.2 mm/mm at -196 °C (**Fig. 6b**). Optical images in **Fig. 6c** confirmed that at higher freezing temperatures (e.g., -25 °C), crack paths appeared straighter and more unstable, while at lower temperatures (e.g., -78 °C and -196 °C), crack paths exhibited more tortuous trajectories, with clear signs of local crack deflection and stretching zones. These trends can be directly linked to the evolution of ice crystal morphology. As confirmed in earlier sections, lower freezing temperatures yield smaller, more densely distributed ice crystals (~4 μm at -196 °C vs. ~50 μm at -25 °C). This finer structure increases the number of crack-bridging sites and promotes energy-dissipating mechanisms such as interfacial debonding and microcrack redirection. These effects collectively enhance fracture resistance and delay catastrophic crack propagation.

Collectively, we hypothetically summarize three primary fracture modes along with crack propagation in frozen double-network (DN) hydrogels: (I) fracture of ice crystals, (ii) delamination at the ice–polymer interface, and (iii) fracture of the polymer

View Article Online
DOI: 10.1039/D5TB02063H

network (**Fig. 6d**). Each of these modes is strongly dependent on the size, distribution, and interfacial behavior of the embedded ice crystals—features that are in turn controlled by freezing temperature and rate. During the fracture of ice crystals (Brittle Ice Phase), in hydrogels frozen at higher subzero temperatures (e.g., -25 °C), large, polycrystalline ice domains are formed. These structures resemble bulk ice, which is inherently brittle due to internal grain boundaries and crystallographic defects[55, 56]. When a propagating crack encounters such large crystals, they fracture catastrophically under localized compressive or shear stresses from the stretched polymer matrix. Although this fracture absorbs some energy, it does not sufficiently blunt or redirect the crack path. Instead, stress concentration at the crack tip remains high, and crack propagation proceeds in a fast and unstable manner—resulting in brittle failure. Thus, while ice fracture contributes to energy dissipation, large ice domains offer limited toughening benefit. For the ice–polymer delamination phase (Interfacial Toughening Phase), as freezing temperature decreases (e.g., -40 °C to -78 °C), ice crystal size decreases and interfacial area between ice and polymer increases. In this regime, ice–polymer interfaces begin to act as crack barriers. When cracks in the polymer network reach the ice domains, interfacial debonding can occur, redirecting or deflecting crack paths. This redirection not only delays catastrophic fracture but also activates interfacial energy dissipation mechanisms—similar to toughening seen in fiber-reinforced or layered composites. The delamination process is especially important in frozen DN hydrogels where covalent crosslinks are absent and network integrity depends on physical interactions. As the crack attempts to pass through or around the ice, local separation consumes energy and reduces crack driving force. Finally, in the polymer network fracture phase (Toughening by Sacrificial Matrix), the final mode involves the failure of the polymer matrix itself. In the absence of reinforcing effects, cracks would propagate directly through the network. However, when frozen at very low temperatures (e.g., -196 °C), the hydrogel contains a dense distribution of small ice crystals (≈4 μm), which significantly alters crack mechanics. Instead of a single dominant crack, the network experiences distributed microcracking, crack tip shielding, and multiple crack branching. These effects lead to a reduction in effective stress concentration and promote a "quasi-ductile" behavior in the frozen material. As seen in both mechanical tests and optical images, these samples show higher strain at break and more gradual failure.

Overall, the toughening of frozen DN hydrogels arises not from a single fracture mode but from the synergistic interplay among ice crystal fracture, ice–polymer interfacial delamination, and polymer network deformation. This interplay is particularly effective in samples containing finely distributed ice crystals and strong interfacial bonding. As the freezing temperature decreases, crack propagation becomes increasingly unstable in a favorable manner—characterized by crack path redirection, growth of delamination zones, and enhanced localized energy dissipation. These cooperative mechanisms lead to notable improvements in fracture strain, crack deflection, and overall material toughness, as demonstrated in the mechanical performance results. In practical terms, the commonly invoked toughening

View Article Online
DOI: 10.1039/D5TB02063H

descriptors—interfacial energy dissipation, localized microcracking, and crack deflection—can each be mapped onto these three damage modes. Interfacial energy dissipation refers to the continuous consumption of mechanical energy through sliding and debonding at ice–polymer boundaries, which becomes increasingly significant as interfacial area grows with finer ice crystals. Localized microcracking describes the spatially distributed micro-damage events that arise when numerous small ice domains and their surrounding polymer matrix undergo concurrent failure, effectively dispersing the stress concentration ahead of the crack tip. Crack deflection refers to the forced redirection of the propagating crack front around heterogeneous ice–polymer regions, producing the tortuous fracture paths observed in **Fig. 6c**. Together, these mechanisms are not independent but rather coupled manifestations of the progressive shift from ice-dominated brittle fracture to interface- and polymer-mediated ductile toughening as ice crystal size decreases.

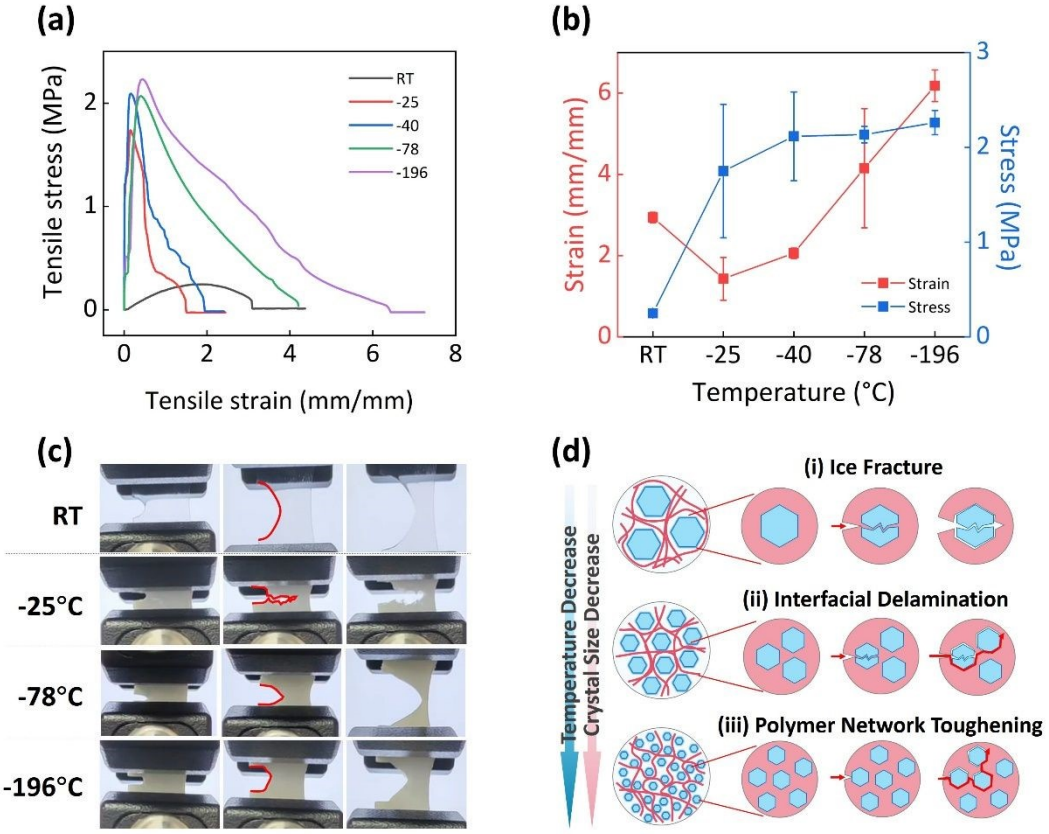

Fig. 6. **(a)** Tensile stress–strain curves of cracked gelatin/pNAGA DN hydrogels frozen at different temperatures. **(b)** Extracted maximum tensile stress (blue) and strain (red) at failure. **(c)** Optical images showing crack propagation behavior during pure shear tests. At room temperature, cracks blunt due to dynamic hydrogen bonding. In frozen hydrogels, lower freezing temperatures promote more tortuous, energy-dissipating crack paths due to finer, more distributed ice crystals. **(d)** Schematic illustration of three primary fracture modes observed in frozen DN hydrogels during crack propagation: (i) fracture of ice crystals, (ii) delamination at the ice–polymer interface, and (iii) fracture of the polymer network. As freezing temperature decreases, the size of ice crystals

View Article Online
DOI: 10.1039/D5TB02063H

reduces and their distribution becomes more uniform. Smaller crystals enhance crack redirection and energy dissipation by increasing interfacial area and reducing stress localization, thereby enabling more stable and tortuous crack propagation and contributing to improved toughness.

While the distinct crack morphologies and proposed fracture modes (**Fig. 6d**) account for the observed toughness enhancement, the underlying mechanisms—particularly interfacial delamination and polymer-network rearrangement—are inherently time-dependent physical processes. Ice crystals fracture rapidly and are largely insensitive to moderate variations in loading rate, whereas interfacial delamination and hydrogen-bond reorganization occur over longer timescales and are therefore expected to exhibit pronounced rate dependence[57, 58]. To further validate the proposed toughening mechanisms and delineate the respective contributions of the three fracture modes, we systematically investigated the rate-dependent mechanical behavior of frozen DN hydrogels using uniaxial tension and pure-shear tests (**Fig. 7**). Under uniaxial tension in **Fig. 7a** and **7b**, increasing the stretch rate from 10 to 300 mm/min raises the apparent modulus from 0.05 MPa to 0.87 MPa, peak stress from 0.75 MPa to 1.7 MPa and reduces the strain at break from 17 mm/mm to 11 mm/mm. At 300 mm/min, the peak stress shows a slight decrease relative to 200 mm/min (~0.95–1.0 MPa), consistent with early instability/necking that truncates stress development. In pure-shear tests (**Fig. 7d** and **7e**), peak stress increases from 2.1 MPa to 4.4 MPa, while maximum stretch collapses, and crack morphology transitions from blunted/tortuous at low rate to sharp/unstable at high rate (**Fig. 7c**). The trends arise because ice–polymer interfacial sliding and H-bond reorganization require time to operate; when the loading timescale shortens, these sacrificial/relaxation pathways are curtailed, producing higher stiffness but reduced crack tolerance.

Mechanistically, ice-enabled toughening in these DN hydrogels arises from three coupled processes: (i) microfracture of confined ice domains, (ii) ice–polymer interfacial delamination/sliding, and (iii) viscoelastic/H-bond reorganization within the polymer networks. These latter two are time-dependent; when loading is fast, interfacial slip and network rearrangement cannot keep pace, the process zone shrinks, stress is carried more directly through the composite, and damage localizes—yielding higher apparent stiffness but reduced crack tolerance and more brittle failure. Under slow loading, interfacial sliding and H-bond exchange proceed, enabling stress redistribution, crack deflection/blunting, and distributed microcracking, which increase energy dissipation and delay catastrophic propagation. Overall, these results confirm that the reinforcement is rate sensitive and governed by rate-limited interfacial and network dynamics.

View Article Online
DOI: 10.1039/D5TB02063H

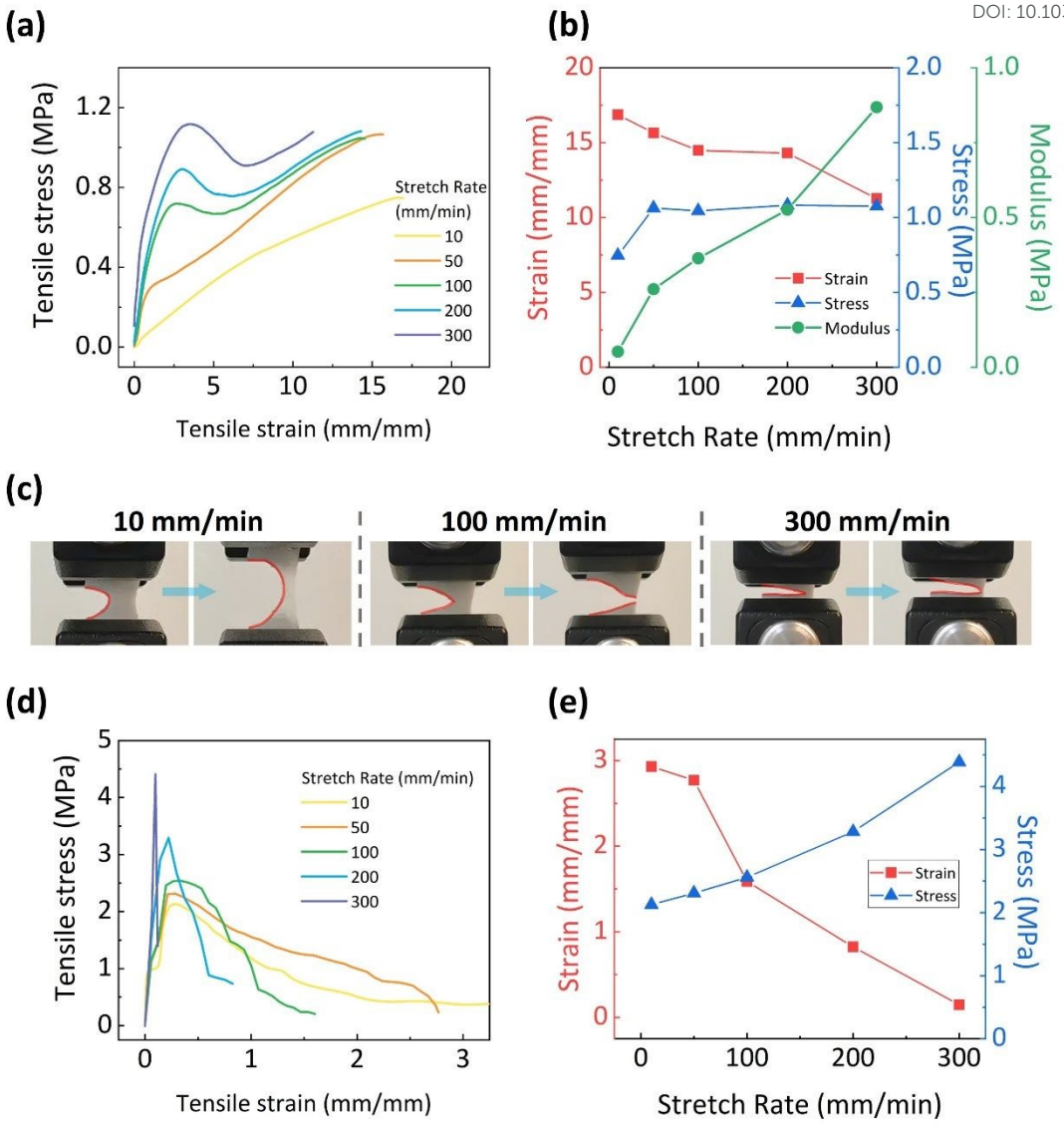

Fig. 7. Stretch-rate dependence of mechanical response in frozen gelatin/pNAGA DN hydrogels prepared at C_{NAGA}=3 M, $C_{gelatin}$=80 mg/mL, frozen at -40 °C. (a) Stress–strain curves at stretch rates of 10, 50, 100, 200, and 300 mm/min. **(b)** Strain at break (red), peak stress (blue) and modulus (green) versus stretch rate. **(c)** Optical views of crack propagation under pure shear at 10, 100, and 300 mm/min, showing a transition from blunted/tortuous to sharp/unstable paths as rate increases. **(d)** Pure-shear stress–strain curves at the same stretch rates. **(e)** Strain at break (left axis) and peak stress (right axis) versus stretch rate for pure-shear tests, indicating rate strengthening accompanied by a strong reduction in allowable stretch.

3.5 Low-Temperature Functionalities of gelatin/pNAGA DN hydrogels

During freezing, the DN hydrogel undergoes a distinct transition driven by ice–polymer phase separation, resulting in reduced local polarity, increased microenvironmental rigidity, and restricted molecular mobility—conditions ideally suited for activating a polarity-sensitive fluorescent reporter. Leveraging this intrinsic behavior, we engineered an embeddable, calibration-free fluorescent indicator for low-

View Article Online
DOI: 10.1039/D5TB02063H

temperature sensing by doping the hydrogel precursor with the polarity-sensitive probe 8-anilino-1-naphthalenesulfonic acid (ANS, 80 μM). As shown in **Fig. 8a,** upon cooling (e.g., to -40 °C), ice formation induces ice-templated microphase separation: water crystallization expels solutes toward polymer-rich regions and creates extended ice–polymer interfaces. ANS molecules are thereby partitioned into more hydrophobic, more rigid microenvironments, which restrict intramolecular rotation and lower local polarity—two effects that strongly enhance ANS emission[59-61]. The material thus switches from weakly fluorescent (nearly no emission under 365-nm UV) at room temperature to bright cyan in the frozen state. Simultaneous infrared thermography shows a close correspondence between surface temperature and fluorescence intensity over the cryogenic window -10 °C to -50 °C, confirming high sensitivity without external power or electronics. Because the switching arises from controlled phase separation, both the threshold temperature and the mechanical profile can be tuned via freezing rate and by modest additions of salts/osmolytes. This simple, biocompatible platform is immediately applicable as an embeddable cryogenic temperature indicator or freeze-state patch for cryobiology, frozen-sample logistics, soft robotics, and cold-chain monitoring.

In addition to serving as a temperature indicator, the subzero physicochemical behavior of the gelatin/pNAGA DN hydrogel highlights its potential as a cytocompatible matrix for mild subzero applications. The hydrogel exhibits a significantly depressed freezing point below −20 °C and thus remains unfrozen and supercooled across a wide temperature window from 0 °C to −20 °C, effectively preventing the formation of damaging extracellular ice. Moreover, both gelatin and pNAGA are inherently biocompatible, enabling the DN hydrogel to function as a cell-friendly matrix suitable for biological use. This property is expected to protect cells by inhibiting the formation of harmful extracellular ice crystals, a primary cause of cell death during conventional cryopreservation. To validate this protective effect, we evaluated the viability of U87MG cells subjected to a freeze–thaw challenge at −20 °C, comparing conditions with and without the hydrogel overlay. As shown in **Fig. 8b** and **8c**, quantitative Live/Dead staining revealed a clear contrast between the two groups. The Control-FT group, exposed directly to the culture medium during freezing, exhibited substantial cell death, with viability decreasing to approximately 75%. In contrast, cells in the Hydrogel-FT group maintained a remarkably high viability of 98%, comparable to the untreated control. This enhanced survival can be attributed to the synergistic protective effects of the DN hydrogel network. First, the hydrogel functions as a supercooled, protective barrier that shields underlying cells from direct ice nucleation and the osmotic stress associated with medium freezing. Second, unlike liquid media, the gelatin-based network provides a stable, biocompatible microenvironment that preserves cell attachment and morphology during thermal stress, preventing detachment commonly observed in freeze–thaw cycles. Collectively, these results confirm that the gelatin/pNAGA DN hydrogel is both cytocompatible and freeze–thaw tolerant, underscoring its potential as a physical matrix for mild subzero biomedical applications, such as cryogenic interfaces, low-temperature processing, and

View Article Online
DOI: 10.1039/D5TB02063H

subzero cell preservation.

To evaluate whether the observed cytoprotective effect is unique to the gelatin/pNAGA DN hydrogel or can also be achieved by other hydrogel systems, we performed a comparative study using four different hydrogels: the gelatin/pNAGA DN hydrogel, the corresponding single-network (SN) hydrogels (SN-gelatin and SN-pNAGA), and a conventional PEGDMA hydrogel. Cell viability and recovery ratio were assessed over 1, 3, and 5 freeze–thaw cycles. The DN hydrogel consistently exhibited the highest protective performance. Cell viability remained above ~90% throughout all five freeze–thaw cycles (**Fig. 8d**, **8e**), indicating a stable and sustained cytoprotective effect. In contrast, both single-network hydrogels showed a rapid decline in protection, with viability decreasing to approximately 10–20% after five cycles. This stark difference can be attributed to the distinct network architectures: the DN hydrogel possesses an interpenetrating dual-network structure in which gelatin triple helices and pNAGA hydrogen-bonding domains cooperatively provide both dense mesh confinement and dynamic stress redistribution, enabling the DN matrix to suppress ice nucleation and restrict ice crystal growth more effectively. Single-network hydrogels lack this cooperative confinement, resulting in greater susceptibility to ice formation and consequently more severe mechanical and osmotic damage to cells. DSC measurements (**Fig. 1b**) further support this interpretation, showing that while all hydrogels exhibit crystallization events in the −20 to −30 °C range, the DN hydrogel's tightly constrained network environment limits the extent and rate of ice crystal growth. For the PEGDMA hydrogel, the protective effect was even weaker—cell viability decreased to nearly zero after several cycles, attributable to its rigid, covalently crosslinked network that lacks the dynamic adaptability to accommodate volumetric changes during ice formation.

The recovery ratio data (**Fig. 8f**) further distinguish the DN hydrogel from the other systems. The DN hydrogel maintained a recovery ratio of ~55–60% across all five cycles, indicating that cells not only survived but also retained attachment on the culture surface. In contrast, SN-pNAGA and PEGDMA hydrogels dropped to near zero after five cycles, and SN-gelatin declined to ~35%—reflecting predominantly cell death rather than adhesion effects, as corroborated by the correspondingly low viability data in Fig. 8e. The moderate recovery ratio of the DN hydrogel (below 100%) is likely related to partial cell adhesion to the gelatin-containing surface, as gelatin inherently contains RGD-like bioactive motifs that promote integrin-mediated cell attachment. However, this adhesion does not progressively worsen across cycles, and in practical cryopreservation scenarios, gentle enzymatic treatment (e.g., trypsinization or collagenase digestion) could release adhered cells to recover the full viable population. For future applications, the adhesion effect could be further mitigated through surface modification with anti-fouling coatings (e.g., zwitterionic or PEG-based layers) or thermoresponsive release mechanisms exploiting the gelatin network's sol–gel transition upon mild warming. Overall, these results demonstrate that the cytoprotective capability is specific to the gelatin/pNAGA DN architecture and cannot be readily

View Article Online
DOI: 10.1039/D5TB02063H

replicated by conventional single-network or covalently crosslinked hydrogels.

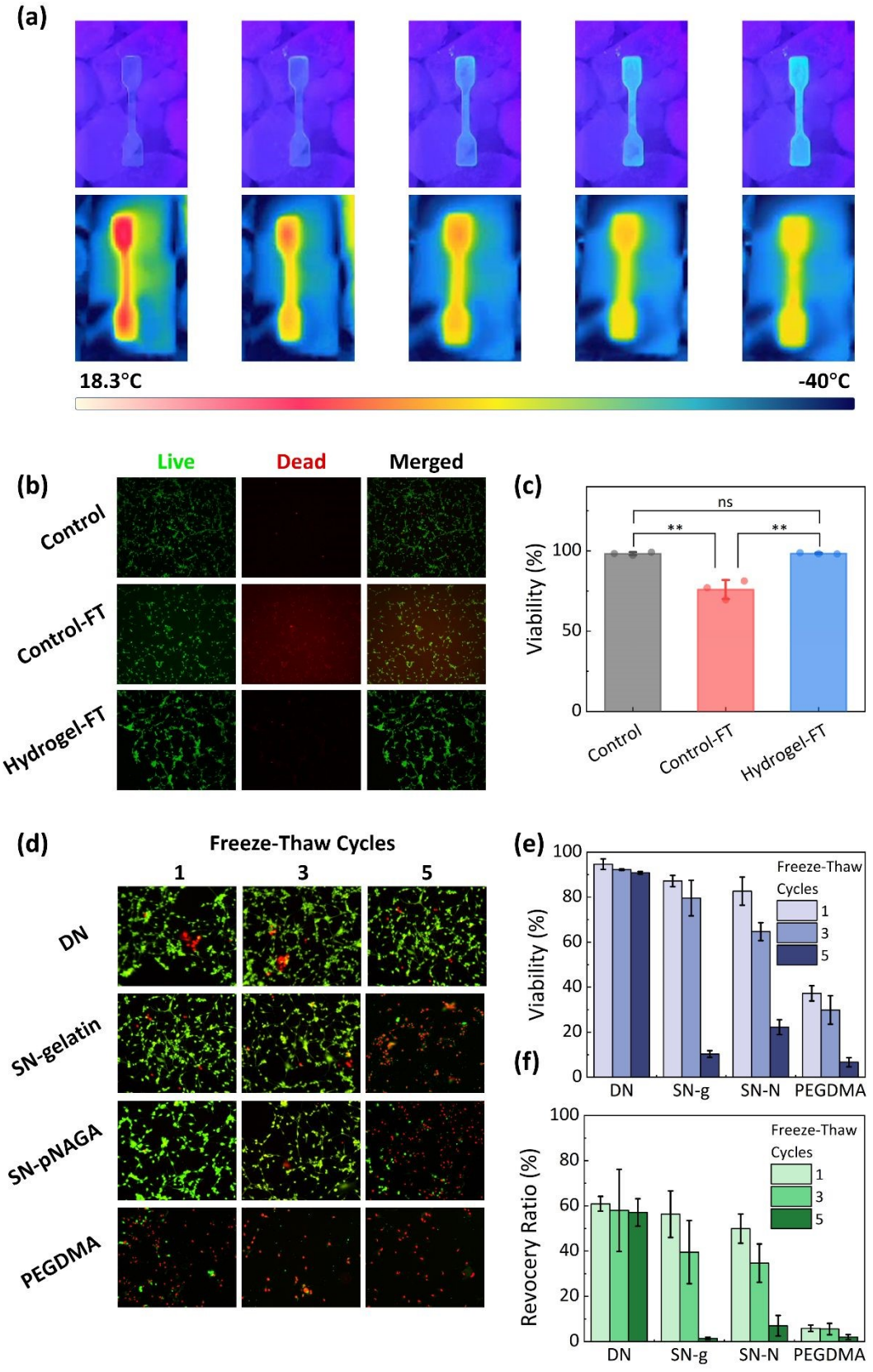

Fig. 8. Gelatin/pNAGA hydrogels for cryogenic applications. (a) Visual and thermal demonstration of reversible cryogenic temperature sensing using an ANS-loaded

View Article Online
DOI: 10.1039/D5TB02063H

gelatin/pNAGA hydrogel. The top row shows photographs under 365 nm UV illumination, and the bottom row displays corresponding infrared thermal images. Upon progressive cooling from 18.3 °C to -40 °C, ice formation induces a dramatic fluorescence turn-on (from nearly dark to bright cyan) that faithfully tracks the temperature drop, illustrating the potential of the frozen hydrogel as a simple, visual sub-zero temperature indicator. **(b)** Representative Live/Dead fluorescence images after thawing, where green and red fluorescence indicate live and dead cells, respectively. U87MG cells cultured in dishes were subjected to a single freeze–thaw cycle (4 °C for 30 min, −20 °C for 1 h, and room temperature for 30 min) either in culture medium alone (Control-FT) or covered with a gelatin/pNAGA hydrogel disc (Hydrogel-FT). **(c)** Quantitative analysis of cell viability. The Hydrogel-FT group exhibited markedly higher viability, attributed to the hydrogel's unfrozen, supercooled state (0 °C to −20 °C) and its intrinsic biocompatibility, which together create a stable, cell-friendly microenvironment during subzero exposure. **(d)** Representative LIVE/DEAD fluorescence images of U87MG cells protected by four hydrogel matrices—gelatin/pNAGA DN, SN-gelatin, SN-pNAGA, and PEGDMA—after 1, 3, and 5 freeze–thaw cycles (−20 °C, 1 h per cycle). Live and dead cells appear green and red, respectively. **(e)** Quantified cell viability as a function of freeze–thaw cycle number for each hydrogel system. DN hydrogel-maintained viability above ~90% through five cycles, whereas SN and PEGDMA hydrogels declined sharply. **(f)** Corresponding recovery ratio, defined as the fraction of cells remaining attached to the culture dish surface after cryoprotection and thawing. Error bars represent standard deviation (n = 3).

To place the mechanical performance of the gelatin/pNAGA DN hydrogel in the broader context of antifreezing hydrogel research, we compiled a comparative analysis against representative systems reported in the literature, categorized by composition: additive-free polymeric hydrogels[48, 62-67], organogels[68-75], protein-assisted hydrogels[76-78], ionic hydrogels[79-90], and nanocomposite hydrogels[91-95] (**Fig. 9 and Table S1**). As shown in **Fig. 9a**, the majority of reported antifreezing hydrogels operate within −40 to 0 °C with moderate extensibility below 1000% strain. In comparison, the present system achieves ~2200% strain at −40 °C and retains substantial stretchability down to −196 °C—a cryogenic regime where very few hydrogels have been tested. The stress–strain map (**Fig. 9b**) further shows that the gelatin/pNAGA DN hydrogel occupies a performance space combining high extensibility with high tensile stress (~2 MPa) that most reported systems cannot access simultaneously. Notably, this performance is achieved entirely without additives, solvents, or nanofillers, confirming that the ice-as-reinforcement strategy introduced in this work represents a fundamentally distinct and competitive design paradigm for antifreezing hydrogels.

View Article Online
DOI: 10.1039/D5TB02063H

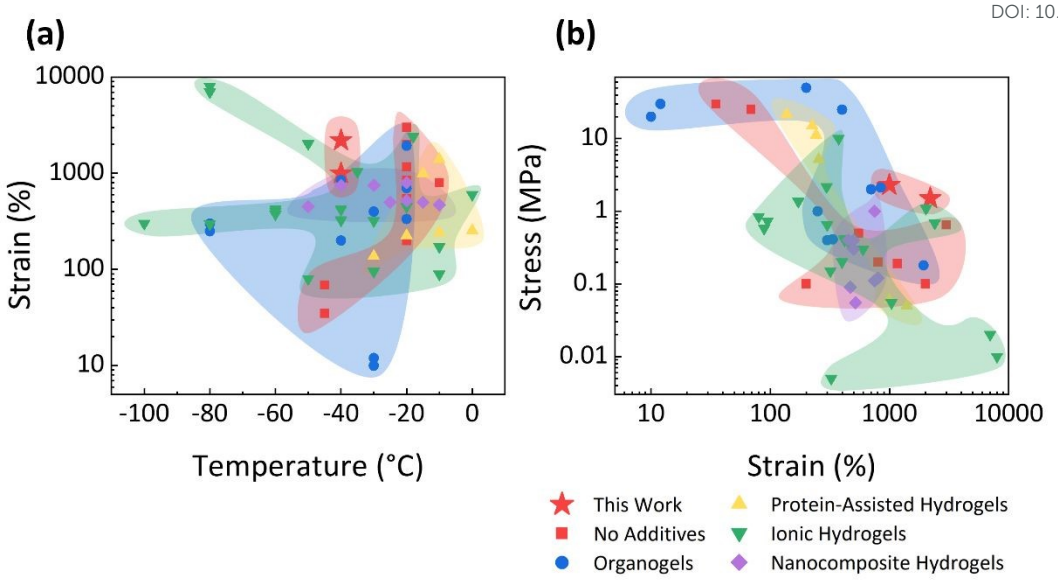

Fig. 9. Comparative performance maps of antifreezing hydrogels reported in the literature, categorized by composition: additive-free polymeric hydrogels (red squares), organogels (blue circles), protein-assisted hydrogels (yellow triangles), ionic hydrogels (green inverted triangles), and nanocomposite hydrogels (purple diamonds). This work is denoted by the red star. **(a)** Tensile strain versus operating temperature. **(b)** Tensile stress versus tensile strain (log–log scale). The gelatin/pNAGA DN hydrogel achieves a combination of high extensibility and high stress that is competitive with or exceeds additive-containing systems, despite relying solely on in situ ice reinforcement without external additives. All references are listed in **Table S1**.

4. Conclusions

In this work, we have developed a new class of frozen hydrogels in which in situ–formed ice crystals function simultaneously as structural templates and reinforcing fillers within a fully physically crosslinked double-network (DN) matrix. This design repurposes ice—from a brittle, damaging phase into a functional toughening component—by confining it within a robust polymer network that supports mechanical reinforcement at subzero temperatures. By systematically tuning freezing parameters, including temperature and duration, we were able to control ice morphology, polymer phase separation, and network densification, which collectively governed the mechanical behavior of the resulting hydrogels. Our findings reveal that freezing time influences ice growth directionality and integration, with an optimal window (~20 minutes at -40 °C) yielding maximal tensile strength and energy dissipation. Freezing temperature, in turn, governs nucleation and crystal size, where lower temperatures produce finer ice domains (~4 μm at -196 °C) that enhance interfacial area, promote tortuous fracture paths, and delay crack propagation. Fracture analyses further identified three synergistic toughening modes—ice crystal fracture, interfacial delamination, and polymer network deformation—that collectively contribute to increased toughness through mechanisms such as interfacial sliding, microcrack deflection, and distributed crack branching.

View Article Online
DOI: 10.1039/D5TB02063H

Together, these results establish a freezing-induced toughening mechanism where ice–polymer interactions convert a traditionally fragile phase into a sacrificial, energy-absorbing material element. This strategy not only eliminates the need for additives, surfactants, or post-synthesis processing but also transforms ice from a design limitation into a performance-enabling phase. Looking ahead, this ice-reinforcement concept lays the foundation for a new generation of soft composites that remain functional under extreme cold, with potential applications in cryo-tolerant biointerfaces, soft robotics, and adaptive materials for polar or extraterrestrial environments.

Acknowledgement. J.Z. thanks financial supports from NSF grant (DMR-2603321) and ACS PRF grant (ND−65277). Edison Liu from Copley High School received research training through this project.

View Article Online
DOI: 10.1039/D5TB02063H

References

1. X. J. Liu, M. Gao, J. Y. Chen, S. Guo, W. Zhu, L. C. Bai, W. Z. Zhai, H. J. Du, H. Wu, C. Z. Yan, Y. S. Shi, J. W. Gu, H. J. Qi and K. Zhou, *Adv. Funct. Mater.*, 2022, **32**, e2203323.

2. M. Neumann, G. di Marco, D. Iudin, M. Viola, C. F. van Nostrum, B. G. P. van Ravensteijn and T. Vermonden, *Macromolecules*, 2023, **56**, 8377-8392.

3. T. Zhu, Y. Ni, G. M. Biesold, Y. Cheng, M. Ge, H. Li, J. Huang, Z. Lin and Y. Lai, *Chem Soc Rev*, 2023, **52**, 473-509.

4. J. Lin, Y. Mao, T. Zheng, Y. Cui, S. Li, Y. Liu, J. Wei, T. Chen and C. Chang, *Adv Mater*, 2025, **37**, e2500949.

5. M. Yao, Z. Wei, J. Li, Z. Guo, Z. Yan, X. Sun, Q. Yu, X. Wu, C. Yu, F. Yao, S. Feng, H. Zhang and J. Li, *Nat Commun*, 2022, **13**, 5339.

6. J. Hu, D. Zhang, W. Li, Y. Li, G. Shan, M. Zuo, Y. Song, Z. Wu, L. Ma, Q. Zheng and M. Du, *ACS Appl Mater Interfaces*, 2024, **16**, 6433-6446.

7. H. Savolainen, N. Hosseiniyan, M. Piedrahita-Bello and O. Ikkala, *Nat Commun*, 2025, **16**, 4544.

8. W. Feng, F. Li, Z. Jiang, C. Yue, G. Yin, N. Zhu, K. Zhang, T. Chen and W. Lu, *Angew Chem Int Ed Engl*, 2025, **64**, e202505192.

9. S. P. Liu, Z. H. Ge, Y. P. Liu, R. Chen, J. X. Xu, Y. X. Zhou, M. Sun, Z. Fan and J. Z. Du, *Adv. Funct. Mater.*, 2025, e09677.

10. H. M. El-Husseiny, E. A. Mady, L. Hamabe, A. Abugomaa, K. Shimada, T. Yoshida, T. Tanaka, A. Yokoi, M. Elbadawy and R. Tanaka, *Mater Today Bio*, 2022, **13**,

View Article Online
DOI: 10.1039/D5TB02063H

100186.

11. X. Xue, Y. Hu, Y. H. Deng and J. C. Su, *Adv. Funct. Mater.*, 2021, **31**, 2009432.

12. D. Zhang, Y. Tang, K. Zhang, Y. Xue, S. Y. Zheng, B. Wu and J. Zheng, *Matter*, 2023, **6**, 1484-1502.

13. H. Yuk, S. Lin, C. Ma, M. Takaffoli, N. X. Fang and X. Zhao, *Nat Commun*, 2017, **8**, 14230.

14. D. Zhang, Y. Tang, Y. Zhang, F. Yang, Y. Liu, X. Wang, J. Yang, X. Gong and J. Zheng, *J. Mater. Chem. A*, 2020, **8**, 20474-20485.

15. D. Zhang, Y. Tang, X. Gong, Y. Chang and J. Zheng, *SmartMat*, 2024, **5**, e1160.

16. O. Y. Dudaryeva, L. Cousin, L. Krajnovic, G. Grobli, V. Sapkota, L. Ritter, D. Deshmukh, Y. Cui, R. W. Style, R. Levato, C. Labouesse and M. W. Tibbitt, *Adv Mater*, 2025, **37**, e2410452.

17. P. He, J. H. Park, Y. Jiao, R. Ganguli, Y. Huang, A. Lee, C. H. Ahn, M. Wang, Y. Peng, Y. Long, C. M. Chen, Z. Wang, Z. Tian, B. Mi, A. C. Arias, C. Fang, A. Toor and L. Lin, *Sci Adv*, 2025, **11**, eadu3711.

18. Y. Yuan, Z. Liu, X. Zou, P. Fang, J. Zhang, Q. Zhang, H. Zhang, Q. Yu, T. Zhou, W. Li, S. Zheng, M. Yang, Z. Sun, M. Zhu and F. Yan, *Nat Mater*, 2025, **24**, 1608-1615.

19. G. W. Liu, M. J. Pickett, J. L. P. Kuosmanen, K. Ishida, W. A. M. Madani, G. N. White, J. Jenkins, S. Park, V. R. Feig, M. Jimenez, C. Karavasili, N. B. Lal, M. Murphy, A. Lopes, J. Morimoto, N. Fitzgerald, J. H. Cheah, C. K. Soule, N. Fabian, A. Hayward, R. Langer and G. Traverso, *Nat Mater*, 2024, **23**, 1292-1299.

20. A. GhavamiNejad, J. F. Liu, S. Mirzaie, B. Lu, M. Samarikhalaj, A. Giacca and X. Y.

View Article Online
DOI: 10.1039/D5TB02063H

Wu, *Nat Commun*, 2025, **16**, 3124.

21. L. L. C. Olijve, K. Meister, A. L. DeVries, J. G. Duman, S. Guo, H. J. Bakker and I. K. Voets, *Proc Natl Acad Sci U S A*, 2016, **113**, 3740-3745.

22. Y. Jian, S. Handschuh-Wang, J. Zhang, W. Lu, X. Zhou and T. Chen, *Mater. Horiz.*, 2021, **8**, 351-369.

23. Y. Zhuo, S. Xiao, V. Håkonsen, J. He and Z. Zhang, *ACS Materials Letters*, 2020, **2**, 616-623.

24. T. Li, H. Wei, Y. Zhang, T. Wan, D. Cui, S. Zhao, T. Zhang, Y. Ji, H. Algadi, Z. Guo, L. Chu and B. Cheng, *Carbohydr. Polym.*, 2023, **309**, 120678.

25. S. Yang, D. Gerber, Y. Feng, N. Bain, M. Kuster, L. de Lorenzis, Y. Xu, E. R. Dufresne and R. W. Style, *Sci Adv*, 2024, **10**, eado7750.

26. X. Liang, G. Chen, I. M. Lei, P. Zhang, Z. Wang, X. Chen, M. Lu, J. Zhang, Z. Wang, T. Sun, Y. Lan and J. Liu, *Adv Mater*, 2023, **35**, e2207587.

27. T. Y. Zhu, D. B. Wang, Y. S. Wang, F. K. Xu, J. Huang, M. Lian, Y. F. Wang, W. Fan, Y. E. Miao, J. X. Zhu, D. H. Nguyen, C. Zhang and T. X. Liu, *Adv. Funct. Mater.*, 2025, **35**, 2503693.

28. S. Miao, Y. Wang, L. Sun and Y. Zhao, *Nat Commun*, 2022, **13**, 4044.

29. S. L. Loo, W. B. Krantz, T. T. Lim, A. G. Fane and X. Hu, *Soft Matter*, 2013, **9**, 224-234.

30. Y. Liu, K. Yuan, Y. Lin, Y. Yang, W. Kong, J. Shan, H. Niu, W. Kong, F. Li, X. Yue, Y. Du, Y. Liang, H. Chang, Z. Yu, J. Wang, G. Yang, L. Cao, K. Huang, S. Yang and T. Tang, *Adv Mater*, 2025, **37**, e2414437.

View Article Online
DOI: 10.1039/D5TB02063H

31. M. V. Dinu, M. Pradny, E. S. Dragan and J. Michalek, *Carbohydr Polym*, 2013, **94**, 170-178.

32. D. Chen, Y. Zhang, C. J. Ni, C. Ma, J. Yin, H. Bai, Y. W. Luo, F. H. Huang, T. Xie and Q. Zhao, *Mater. Horiz.*, 2019, **6**, 1013-1019.

33. M. Hua, S. Wu, Y. Ma, Y. Zhao, Z. Chen, I. Frenkel, J. Strzalka, H. Zhou, X. Zhu and X. He, *Nature*, 2021, **590**, 594-599.

34. S. He, W. Liang, Y. Tang, J. Zhang, R. Wang, L. Quan, Y. Ouyang, R. Huang, R. Dou and D. Wu, *Nat Commun*, 2025, **16**, 3198.

35. Y. B. Xu, J. J. Tan, W. L. Dong, Y. N. Chen, Y. Wuliu, W. J. Xu, R. X. Wang, G. Yin, Z. L. Zhang, C. Z. Zhu, J. Xu and L. Tian, *Adv. Funct. Mater.*, 2025, **35**, 2419161.

36. W. Gu, S. Yang, D. Zhao, Y. Zou, C. Chen, P. Niu, X. Liang, C. T. Kwok, B. Zhou, C. Wang, Y. Y. S. Huang, J. Liu and I. M. Lei, *Sci Adv*, 2025, **11**, eadv7786.

37. I. N. Savina, G. C. Ingavle, A. B. Cundy and S. V. Mikhalovsky, *Sci Rep*, 2016, **6**, 21154.

38. K. Zhang, Z. Yang, M. P. Seitz and E. Jain, *ACS Appl Bio Mater*, 2024, **7**, 5925-5938.

39. M. Si, Y. Tang, C. Xu, C. Y. Li, K. Xia, W. Xu, J. Lin, Z. Jiang, J. Yang and S. Y. Zheng, *Mater Horiz*, 2025, **12**, 1452-1462.

40. P. Rao, T. F. Li, Z. L. Wu, W. Hong, X. X. Yang, H. H. Yu, T. W. Wong, S. X. Qu and W. Yang, *Extreme Mech. Lett.*, 2019, **28**, 43-49.

41. A. Alam, Y. J. Zhang, H. C. Kuan, S. H. Lee and J. Ma, *Prog. Polym. Sci.*, 2018, **77**, 1-18.

42. N. S. Dzulkharnien and R. Rohani, *Journal*, 2022, **12**, 1629.

View Article Online
DOI: 10.1039/D5TB02063H

43. Y. Wang, M. Zhang, Z. Yan, S. Ji, S. Xiao and J. Gao, *Theranostics*, 2024, **14**, 1534-1560.

44. C. Chen, L. Berglund, I. Burgert and L. Hu, *Adv Mater*, 2021, **33**, e2006207.

45. S. De, S. J. Rukmani, X. Zhao, C. Clarkson, F. Vautard, S. Bhagia, M. Goswami, S. Zhang, S. F. Elyas, W. Zhao, J. C. Smith, A. J. Ragauskas, S. Ozcan, H. Tekinalp, M. Si, J. Huang and X. He, *Adv. Funct. Mater.*, 2024, **35**, 2414222.

46. J. J. Petrovic, *J. Mater. Sci.*, 2003, **38**, 1-6.

47. Q. Chen, L. Zhu, C. Zhao, Q. Wang and J. Zheng, *Adv Mater*, 2013, **25**, 4171-4176.

48. D. Zhang, Y. Liu, Y. Liu, Y. Peng, Y. Tang, L. Xiong, X. Gong and J. Zheng, *Adv Mater*, 2021, **33**, e2104006.

49. X. Dai, Y. Zhang, L. Gao, T. Bai, W. Wang, Y. Cui and W. Liu, *Adv Mater*, 2015, **27**, 3566-3571.

50. X. Liang, G. Chen, S. Lin, J. Zhang, L. Wang, P. Zhang, Z. Wang, Z. Wang, Y. Lan, Q. Ge and J. Liu, *Adv Mater*, 2021, **33**, e2102011.

51. H. Bai, A. Polini, B. Delattre and A. P. Tomsia, *Chem Mater*, 2013, **25**, 4551-4556.

52. G. Shao, D. A. H. Hanaor, X. Shen and A. Gurlo, *Adv Mater*, 2020, **32**, e1907176.

53. D. Xu, X. Meng, S. Liu, J. Poisson, P. Vana and K. Zhang, *Nat Commun*, 2024, **15**, 6886.

54. K. G. Libbrecht, *Annual Review of Materials Research, Vol 47*, 2017, **47**, 271-295.

55. E. M. Schulson, *Jom-Journal of the Minerals Metals & Materials Society*, 1999, **51**, 21-27.

56. E. M. Schulson, *Acta Metall. Mater.*, 1990, **38**, 1963-1976.

View Article Online
DOI: 10.1039/D5TB02063H

57. R. Bai, J. Yang, X. P. Morelle, C. Yang and Z. Suo, *ACS Macro Lett*, 2018, **7**, 312-317.

58. Y. J. Wang, C. Y. Li, Z. J. Wang, Y. P. Zhao, L. Chen, Z. L. Wu and Q. Zheng, *Journal of Polymer Science Part B-Polymer Physics*, 2018, **56**, 1281-1286.

59. A. J. Guliyeva and O. K. Gasymov, *Biochem Biophys Rep*, 2020, **24**, 100843.

60. H. Lei, L. Dong, Y. Li, J. Zhang, H. Chen, J. Wu, Y. Zhang, Q. Fan, B. Xue, M. Qin, B. Chen, Y. Cao and W. Wang, *Nat Commun*, 2020, **11**, 4032.

61. E. Schonbrunn, S. Eschenburg, K. Luger, W. Kabsch and N. Amrhein, *Proc Natl Acad Sci U S A*, 2000, **97**, 6345-6349.

62. M. Wu, C. Y. Qiao, P. F. Sui, J. L. Luo, Z. L. Li, Y. Cao, R. J. Pei, X. W. Peng and H. B. Zeng, *Adv. Funct. Mater.*, 2025, **35**.

63. X. Zhang, Y. Lin, S. Shen, Z. Du, Z. Lin, P. Zhou, H. Huang, X. Lyu and Z. Zou, *Adv Mater*, 2025, **37**, e2413856.

64. H. Yin, M. You, X. Shi, H. Yu and Q. Chen, *Mater Horiz*, 2024, **11**, 3946-3960.

65. L. X. Hou, H. Ju, X. P. Hao, H. Zhang, L. Zhang, Z. He, J. Wang, Q. Zheng and Z. L. Wu, *Adv Mater*, 2023, **35**, e2300244.

66. X. Liu, X. Ji, R. Zhu, J. Gu and J. Liang, *Adv Mater*, 2024, **36**, e2309508.

67. G. P. Wang, H. C. Ni, Y. F. Li, H. Torun, S. Chen, M. W. Shahzad, X. H. Zhang, S. Y. Zheng, B. B. Xu and J. T. Yang, *Adv. Funct. Mater.*, 2025, **35**.

68. S. Wu, Z. Liu, C. Gong, W. Li, S. Xu, R. Wen, W. Feng, Z. Qiu and Y. Yan, *Nat Commun*, 2024, **15**, 4441.

69. Y. C. Yan, S. D. Duan, B. Liu, S. W. Wu, Y. Alsaid, B. W. Yao, S. Nandi, Y. J. Du, T.

View Article Online
DOI: 10.1039/D5TB02063H

W. Wang, Y. Z. Li and X. M. He, *Adv. Mater.*, 2023, **35**.

70. W. L. Zhang, H. J. Zhang, L. B. Li, Q. Wang, W. Wang, L. Xing, P. Fatehi and X. Y. You, *Small*, 2026, **22**.

71. Y. L. Wang, Z. L. Wang, Y. J. Zhang, J. W. Yang, Z. M. Zhang, P. C. Zhou, Y. M. Xu, Q. Y. Sun, M. Q. Zheng, W. Q. Yan, X. Z. He, J. Y. Chen, J. Li, Y. H. Jiang, S. H. Lee, H. Haick, T. Yokota, T. Someya and Y. Wang, *Sci. Adv.*, 2025, **11**.

72. A. Georgopoulou, S. Lee, B. H. Dai, F. Bono, J. Hughes and E. Amstad, *Commun. Mater.*, 2025, **6**.

73. Z. Y. Cao, C. F. Han, Y. L. Zhao, Z. T. Wang, K. K. Zhou, Y. J. Zhang, W. Zhai, G. Q. Zheng, C. F. Pan, K. Dai, C. T. Liu and C. Y. Shen, *Adv. Funct. Mater.*, 2025, DOI: 10.1002/adfm.202529024.

74. Y. D. Shi, Y. J. Guan, M. J. Liu, X. C. Kang, Y. Tian, W. C. Deng, P. Yu, C. Y. Ning, L. Zhou, R. M. Fu and G. X. Tan, *ACS Nano*, 2024, **18**, 3720-3732.

75. M. F. Chen, J. Z. Chen, W. J. Zhou, X. Han, Y. G. Yao and C. P. Wong, *Adv. Mater.*, 2021, **33**.

76. H. Z. Du, X. F. Chen, H. X. Gong, Y. D. Pang, K. Yang, Z. M. Wang, C. Gao, B. X. Lin and Z. Y. He, *Angew Chem Int Edit*, 2025, **64**.

77. J. Xu, R. Jing, X. Ren and G. Gao, *J. Mater. Chem. A*, 2020, **8**, 9373-9381.

78. Y. Wang, Y. Xia, P. Xiang, Y. Dai, Y. Gao, H. Xu, J. Yu, G. Gao and K. Chen, *Chem. Eng. J.*, 2022, **428**.

79. X. F. Pan, J. W. Pan, X. Li, Z. K. Wang, Y. H. Ni and Q. H. Wang, *Adv. Mater.*, 2024, **36**.

View Article Online
DOI: 10.1039/D5TB02063H

80. X. Zhang, D. Li, X. Yang, L. Wang, G. Li, T. W. Wong, T. Li, W. Yang and Z. Luo, *Science*, 2025, **387**, 967-973.

81. S. W. Huang, L. Hou, T. Y. Li, Y. C. Jiao and P. Y. Wu, *Adv. Mater.*, 2022, **34**.

82. S. W. Wu, T. W. Wang, Y. J. Du, B. W. Yao, S. D. Duan, Y. C. Yan, M. T. Hua, Y. Alsaid, X. Y. Zhu and X. M. He, *NPG Asia Mater.*, 2022, **14**.

83. C. Wang, Y. Liu, X. C. Qu, B. J. Shi, Q. Zheng, X. B. Lin, S. Y. Chao, C. Y. Wang, J. Zhou, Y. Sun, G. S. Mao and Z. Li, *Adv. Mater.*, 2022, **34**.

84. Q. Yang, W. J. Yang, Z. Wang, R. Chen, M. Z. Li, C. J. Qin, D. H. Gao and W. Chen, *ACS Appl. Mater. Interfaces*, 2023, **15**, 51684-51693.

85. W. Q. Wang, Y. Z. Liu, S. Q. Wang, X. M. Fu, T. C. Zhao, X. Chen and Z. Z. Shao, *ACS Appl. Mater. Interfaces*, 2020, **12**, 25353-25362.

86. S. H. Jiang, J. J. Deng, Y. H. Jin, B. Qian, W. Q. Lv, Q. Q. Zhou, E. H. Mei, R. E. Neisiany, Y. H. Liu, Z. W. You and J. Pan, *Bioact. Mater.*, 2023, **21**, 313-323.

87. J. B. Yang, Z. Xu, J. J. Wang, L. G. Gai, X. X. Ji, H. H. Jiang and L. B. Liu, *Adv. Funct. Mater.*, 2021, **31**.

88. M. L. Yu, H. Y. Zhang, Q. N. Yang, N. Li, J. J. Du, L. J. Xu and J. X. Xu, *Chem. Eng. J.*, 2025, **505**.

89. Q. J. Fu, S. W. Hao, L. Meng, F. Xu and J. Yang, *ACS Nano*, 2021, **15**, 18469-18482.

90. N. He, B. S. Wang, X. S. Sun, Q. W. Gao, X. Y. Xu, Y. F. Yang, F. G. Dong, J. Miao, H. A. Wang, D. W. Tang and L. Li, *Nat. Commun.*, 2026, **17**.

91. J. X. Li, S. N. Shi, W. X. Wang, L. J. Bai, H. Chen, K. Wei and L. X. Yang, *Chem. Eng. J.*, 2025, **524**.

View Article Online
DOI: 10.1039/D5TB02063H

92. X. Gao, J. Wu, Y. Wang, Y. Wang, Y. Zhang, T. T. Nguyen and M. Guo, *Int J Biol Macromol*, 2024, **265**, 131118.

93. W. J. Ge, S. Cao, Y. Yang, O. J. Rojas and X. H. Wang, *Chem. Eng. J.*, 2021, **408**.

94. J. Yu, Y. F. Feng, D. Sun, W. F. Ren, C. Y. Shao and R. C. Sun, *ACS Appl. Mater. Interfaces*, 2022, **14**, 10886-10897.

95. L. Han, K. Z. Liu, M. H. Wang, K. F. Wang, L. M. Fang, H. T. Chen, J. Zhou and X. Lu, *Adv. Funct. Mater.*, 2018, **28**.

View Article Online
DOI: 10.1039/D5TB02063H

Data Availability Statement

All data supporting the findings of this study are available within the main manuscript and the accompanying Electronic Supplementary Information (ESI).